2007-03-20

The Effects of Vortex Generator Jet Frequency, Duty Cycle, and Phase on Separation Bubble Dynamics

Matthew J. Bloxham
Brigham Young University - Provo

THE EFFECTS OF VORTEX GENERATOR JET FREQUENCY,

DUTY CYCLE, AND PHASE ON SEPARATION

BUBBLE DYNAMICS

by

Matthew Jon Bloxham

A thesis submitted to the faculty of

Brigham Young University

in partial fulfillment of the requirements for the degree of

Master of Science

Department of Mechanical Engineering

Brigham Young University

April 2007

BRIGHAM YOUNG UNIVERSITY

GRADUATE COMMITTEE APPROVAL

of a thesis submitted by

Matthew Jon Bloxham

This thesis has been read by each member of the following graduate committee and by majority vote has been found to be satisfactory.

Date	Jeffrey P. Bons, Chair

Date	R. Daniel Maynes

Date	Deryl O. Snyder

BRIGHAM YOUNG UNIVERSITY

As chair of the candidate's graduate committee, I have read the thesis of Matthew Jon Bloxham in its final form and have found that (1) its format, citations, and bibliographical style are consistent and acceptable and fulfill university and department style requirements; (2) its illustrative materials including figures, tables, and charts are in place; and (3) the final manuscript is satisfactory to the graduate committee and is ready for submission to the university library.

_____	_____
Date	Jeffrey P. Bons
	Chair, Graduate Committee

Accepted for the Department

_____
Matthew R. Jones
Graduate Coordinator

Accepted for the College

_____
Alan R. Parkinson
Dean, Ira A. Fulton College of Engineering and Technology

ABSTRACT

THE EFFECTS OF VORTEX GENERATOR JET FREQUENCY,

DUTY CYCLE, AND PHASE ON SEPARATION

BUBBLE DYNAMICS

Matthew Jon Bloxham

Department of Mechanical Engineering

Master of Science

Vortex generator jets (VGJs) have proven to be effective in minimizing the separation losses on low-pressure turbine blades at low Reynolds numbers. Experimental data collected using phase-locked particle image velocimetry and substantiated with a hot-film anemometer were used to answer fundamental questions about the influence of VGJs on a separated boundary layer. The data were collected on the suction surface of the Pack B blade profile, which has a non-reattaching separation bubble beginning at 68% axial chord. Two VGJ pulse histories were created with different frequencies, jet durations, and duty cycles. The mechanisms responsible for boundary layer separation control were shown to be a combination of boundary layer transition and streamwise vortical

structures. Jet duration and relaxation time were important VGJ characteristics in determining the extent of control.

The unsteady environment characterisitic of the low-pressure turbine section in a gas turbine engine effectively reduces the time-averaged separation zone by as much as 35%. Upstream blade rows create unsteady flow disturbances (wakes) that transition the flow. This transitioned flow propagates downstream, re-attaching the separation bubbles on the subsequent blade row. Phase-locked PIV and hot-film measurements were used to document the characteristics of this separation zone when subjected to synchronized unsteady wakes and VGJs. The phase difference between VGJ actuation and the wake passing, blowing ratio, and VGJ duration were optimized to achieve the greatest time-averaged control of the separation zone. The experimental data were used to identify the important characteristics of the wake/jet interaction. Phase-locked PIV measurements were taken to isolate the wake event (wake only), the VGJ event (jets only), and the synchronized combination of unsteady wakes and jets. The synchronized conditions achieved maximum separation bubble control. The presence of wake and jet induced calmed zones are also noted.

ACKNOWLEDGMENTS

TABLE OF CONTENTS

LIST OF TABLES

LIST OF FIGURES

xii

NOMENCLATURE

B   blowing ratio ($U_{jet}/U_{e\,@\,59\%\,Cx}$) [use U_{max} if pulsed VGJs]

C_x axial chord (24cm)

Cp   pressure coefficient ($P_{Tot,in}$-P)/($P_{Tot,in}$-$P_{S,in}$)

DC   duty cycle

F^+ dimensionless forcing frequency (f/(U_{avg}/SSLJ))

FFT   fast Fourier transform

L   distance between rods

LPT   low-pressure turbine

P   pressure

Re_c Reynolds number based on inlet velocity and axial chord ($C_x U_{in}/\nu$)

SSLJ   suction surface length from jet location to the trailing edge

U   velocity magnitude

U_{avg} average freestream velocity from jet location to the trailing edge

T   rod passing period (225 ms)

W   full wake of the LPT

d   jet hole diameter (2.6mm)

f   VGJ forcing frequency

s   blade spacing

t   time (seconds)

u   x-component of velocity (approximately streamwise)

u uncertainty

v   y-component of velocity (approximately blade normal)

w   z-component of velocity (spanwise)

x   approximate streamwise coordinate

y   approximate blade normal coordinate

z   spanwise coordinate (z = 0 at bottom of VGJ hole)

δ boundary layer thickness

φ flow coefficient ($U_{in,axial}/U_{rod}$)

Γ integrated boundary layer momentum flux loss

ν kinematic viscosity

subscripts

axial   axial direction

e   boundary layer edge

in   cascade inlet conditions

jet   VGJ jet

max   maximum

o   baseline case without wakes or VGJ control

rod   wake generator rod

rms   root mean square

wake   wake data set

3Hz   3Hz data set

5Hz   5Hz data set

S   Static

Tot   Total

1 Introduction

Low pressure turbine blades are designed to be highly loaded (cause maximum turning) during takeoff conditions and provide sufficient power during high altitude flight (low Re). This range of flight requirements makes it difficult to create LPT blades that operate efficiently over the duration of the flight. LPT blades are prone to have boundary layer separation during low Re flight conditions[1-4]. This boundary layer separation greatly increases the losses of the turbine. Sharma et al.[3] measured a 300% increase in the loss coefficient with Re lower than 95K. These results were substantiated by Matsunuma et al.[4] in a study of land based turbines at Re below 65K. Both passive and active flow control strategies have been studied in detail with the objective of eliminating this low Re boundary layer separation.

1.1 Passive Control

Passive control systems are labeled "passive" because they require no external energy sources and, once implemented, continually affect the flow. They are sometimes simplistic devices which are easily integrated into the LPT. Lake et al.[5] studied the effects of boundary layer trips and dimples on a separating boundary layer. They showed that these passive techniques are effective methods of eliminating the separation region in low Re conditions. Passive control systems also have their disadvantages. Given that these

systems require physical adaptations to the LPT blade, their impact is evident across the full range of flight conditions. These systems have a negative impact at higher Re conditions (cause higher losses).

1.2 Active Control

Active control systems require an outside source of energy. These systems include plasma actuators, MEMs actuators, heated wires, and vortex generator jets. Implementing active systems is much more involved than a passive system, requiring internal adaptations to the blades and an external power source. Active systems also have their advantages. They are adaptable to any range of flight conditions. When they are not needed they can be disengaged, thereby eliminating adverse effects during optimal flight conditions.

1.3 Vortex Generator Jets

Vortex generator jets have shown considerable promise as an active flow control system. VGJs could be implemented into low-pressure turbine blades using a manufacturing process similar to the process used to create film cooling systems. This is advantageous given that this process has been established. The VGJs could use bleed air from the bypass duct of a common turbofan engine. VGJs have proven to be effective at curbing separation for both steady and unsteady applications.

In steady applications the VGJ produces a streamwise vortex pair. The vortices are of opposite sign and varying magnitude. The dominant vortex pulls high momentum freestream fluid into the separated boundary layer effectively reenergizing the flow.[7,8]

2

This control has been shown for a wide range of blowing ratios ($U_{jet}/U_{e \ @ \ 59\% \ Cx}$). Although the mass flow requirements for steady jets are small, unsteady jets have been shown to curb the separation but at a fraction of the mass flow requirements.

Experiments have also shown that pulsed vortex generator jets are effective at controlling boundary layer separation for a wide range of operating parameters. The mechanisms of control for pulsed VGJs are currently not completely understood. Computational studies performed by Postl et al.[9] suggested that the primary mechanism of control for unsteady VGJs was due to boundary layer transition rather than streamwise vortical structures. These results were obtained at VGJ blowing ratios below unity. Postl et al. did note that vortical structures began to play a more important role as the blowing ratios were increased. They also noted the formation of a 2D (spanwise) disturbance in the separation bubble. This disturbance formed after VGJ actuation and helped to accelerate reattachment.

Bons et al.[10] studied the impact of unsteady VGJs on a separation bubble using the Pack B blade profile. They used boundary layer traverses and static pressure taps to monitor the changes in the separation zone with both steady and unsteady VGJ control. They reported reductions in the wake loss profile of over 50% with unsteady control, which was later substantiated by the results of Volino[11] obtained using synthetic jets. The unsteady result obtained by Bons et al. compared favorably to the control achieved with steady VGJs but at a fraction of the mass flow requirements. These results were obtained over a range of forcing frequencies and duty cycles with the conclusion that both variables had little impact on the time-averaged wake losses. The forcing frequency independence was demonstrated over a forcing frequency range of $0.1 < F^+ < 7.7$. The

dimensionless forcing frequency was defined by Bons et al. as the VGJ forcing frequency normalized by the ratio of average freestream velocity (from the jet location to the trailing edge) to the suction surface length (from the jet location to the trailing edge). Bons et al. further showed that the extent of the control was more profoundly impacted by the starting and ending of the jet pulse rather than the amount of time the jet remained active.

1.4   Unsteady Wakes

Previous work with LPT flow control has been conducted in steady flow cascades without accounting for the unsteady nature of the flow in an actual engine. In a low-pressure turbine, unsteady disturbances are continually produced by the upstream blade row. Unsteady wakes have been shown to re-energize separation regions as they convect downstream. Stieger et al.[12] attributed this effect to boundary layer embedded vortical structures. They first noted large amplitude pressure fluctuations as a result of these wake-induced vortical structures. Later, these structures were identified using particle image velocimetry. Stieger et al. hypothesized that these vortical structures were created by a rollup of the separated shear layer induced by the wake disturbance.

Gostelow et al.[13] also observed this effect using wake disturbed flow over a flat plate with an imposed pressure distribution. The pressure distribution was representative of the diffusion distribution seen on a compressor blade and encouraged the development of a laminar separation bubble. An upstream rod, parallel with the leading edge of the flat plate, was fastened to a rotating disc. The disc rotated at a rate of 60 rpm, thereby creating two different wakes (one from the rod at an upstream location and the second

4

from a downstream location) every second. Gostelow et al. collected their data by traversing a single element hot-wire through the separation bubble at discrete locations. They showed that the wake-induced disturbance stabilized the boundary layer. The wake-induced disturbance was followed by a calmed region that delayed transition and stabilized the boundary layer against separation. Figure 1-1 contains a plot presented by Gostelow et al. which depicts this calmed zone.
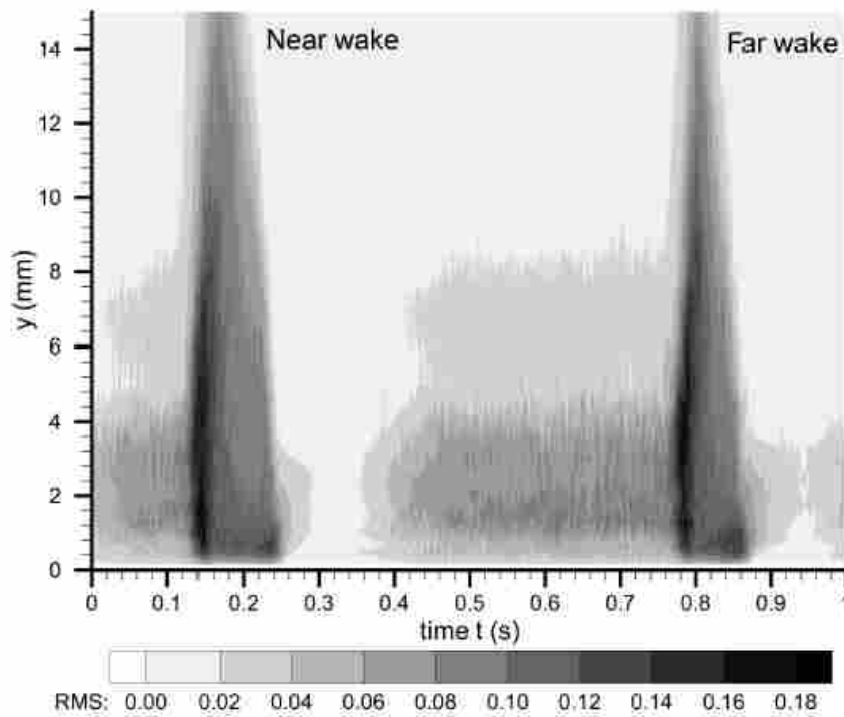
Figure 1-1: Time history plot of U_{rms} velocity at one streamwise location. The effects of both wake disturbances are presented.

The plot is a time history of U_{rms} collected at one streamwise location. The wake disturbances are characterized by elevated regions of U_{rms} which span the plot in the wall normal direction (y). The near wake disturbance is present near a time of 0.14 seconds.

Following this wake disturbance, the velocity fluctuations decrease indicating a "calmed zone". This result was further substantiated by similar studies recently performed by Funazaki et al.[14] and Cattanei et al.[15]

1.5 Synchronized Wakes/Active Control (VGJs)

Given the well documented effects of wakes on separated flows, it is clear that any active flow control scheme must be compatible with the inherently unsteady flow environment in the low-pressure turbine. To date, the synchronization of unsteady wakes and unsteady control had not previously been investigated. This synchronization study could potentially allow for more highly loaded turbine blades with imbedded flow control, effectively reducing the number of necessary blade rows.

1.6 Research Objectives

The objectives of this research are presented in the following numerical list.

1. Identify the role of VGJ actuation and relaxation time in separation bubble control. In order to accomplish this task, the effects of two distinct jet histories were considered. The jet histories were carefully selected to isolate the effects of two different frequencies and duty cycles on the separated boundary layer. This objective was accomplished using particle image velocimetry (PIV).

2. Identify the mechanisms of control responsible for boundary layer reattachment. This objective was accomplished using predominantly PIV data. The results and conclusions are further supported with hot-film data.

3. Identify a blowing ratio, jet duration, and synchronization between the unsteady wake disturbance and the unsteady jet disturbance that cause the greatest time-averaged reduction of the separation bubble. This objective was accomplished using static pressure taps and boundary layer data obtained with a single element hot-film.

4. Upon completion of the optimization study, phase-locked and time-resolved PIV and hot-film data were taken to identify the relative impacts of the two unsteady disturbances and to identify the flow physics that determined the optimal conditions.

2   Experimental Configuration

2.1   Wind Tunnel

A detailed description of the cascade facility used for this study is found in Eldredge and Bons[16]. The open-loop wind tunnel is powered by a centrifugal blower. After passing through a series of flow conditioners, the air enters an acrylic duct with a velocity uniformity of ±2%. The duct is acrylic to allow for optical access and has a cross-sectional area of 0.37 m^2. A square-bar passive grid is placed 5.2 axial chords upstream of the test section to produce 3% freestream turbulence at the cascade inlet.

2.1.1   Linear Cascade

The test section is a two passage, linear cascade containing the Pratt & Whitney Pack B blade configuration. The Pack B is a highly loaded, experimental blade profile. A depiction of the cascade is found in Figure 2-1. The Pack B blade has an axial chord of 0.238m, a span of 0.38 m, a design Zweifel coefficient of 1.15, and provides a cascade solidity of 1.14. At Reynolds numbers below 20,000 (based on inlet velocity and axial chord), a non-reattaching separation bubble forms on the aft portion of the blade beginning near 68% Cx. The inlet velocity was measured using a pitot tube.
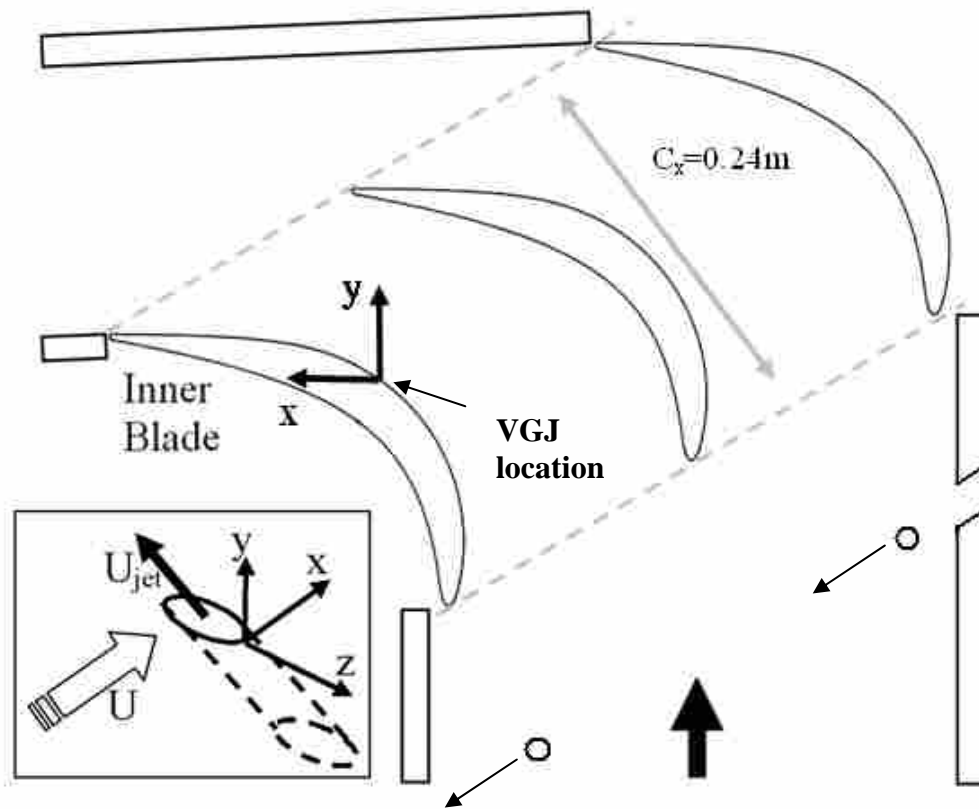
Figure 2-1: Three blade linear cascade. Inset (bottom left corner) depicts coordinate system of the vortex generator jet.

2.1.2   Inner Blade

The innermost blade in the cascade contains 13 static pressure taps. The taps are located near mid-span and are used to provide a Cp profile of the suction surface of the blade. The Cp profile is produced by sequentially connecting these pressure taps to a 0.1" H_2O Druck differential pressure transducer referenced to a pitot tube located upstream of the cascade inlet. This differential pressure is then divided by the dynamic pressure at the inlet to yield Cp. The resulting Cp distribution was compared to the prediction generated

10

by the Air Force Research Laboratory using a 2D viscous solver (VBI, Rao et al.[17]). After the blades were geometrically positioned, adjustments in the location of the tailboards and inlet bleeds were made to most nearly approximate the VBI solution at high (non-separating) Reynolds numbers.

Data were collected on the suction surface of the inner blade of the cascade. This blade doesn't have a true wake, since it is not fully immersed in the flow. Despite this, the inner blade is the preferred control blade since it experiences the design uncovered turning near the trailing edge. The middle blade of the cascade is influenced by the wall that runs from the trailing edge of the outside blade to the end of the tunnel. This wall helps to turn the flow thereby inhibiting boundary layer separation on the middle blade.

The inner blade of the cascade houses a pressure cavity which connects to a spanwise row of vortex generator jets (VGJs). These jets are 2.6 mm in diameter (d) and are spaced 10d apart along the full span of the blade at 59% C_x. The jets are injected into the flow at a 30° pitch angle and a 90° skew angle to the flow as seen in the inset of Figure 2-1. The pressure cavity is connected to high pressure air with an inline solenoid valve that regulates the shape of the VGJ profile (jet duration and duty cycle). The solenoid valve is controlled by a Parker Hannifin pulse driver. The pulse driver can be used to manipulate the amount of time the solenoid valve is open or closed. The pulse driver operates with an internal or external trigger. When the VGJs are being used exclusively the pulse drive is set on internal mode. When the wake generator is active the pulse driver is set on external mode.

2.2   VGJ Pulse Histories

The VGJ pulse histories used in this study were defined by the blowing ratio, duty cycle, and frequency. Blowing ratios (B_{max}) of 2 and 2.5 were used, where the blowing ratio is defined as the ratio of the jet exit velocity to the local freestream velocity ($B_{max}=U_{jet}/U_{e\ @\ 59\%\ Cx}$). The VGJ duty cycle (DC) is defined as the ratio of the amount of time the jet is active to the total period of the VGJ.

Jet profiles were measured as the VGJ exited the blade into a quiescent environment using a single element hot-film anemometer positioned normal to the jet exit. The position of the hot-film was adjusted until the maximum velocity was found. This was done using a three axis traverse located above the tunnel. This traverse allowed for movements as small as 0.1 mm. After the maximum location was found, the cavity pressure was adjusted with an inline valve until the desired blowing ratio was achieved. Twenty profiles were taken and averaged together to obtain the average jet profiles. These profiles are essentially step functions with the initial, high-frequency oscillations attributed to the compressibility of the air in the pressurized cavity. Four different pulse histories were used to meet the objectives of this thesis. While the jet profiles were being measured an inline pressure regulator was used to record the line pressure. The line pressure could then be matched to obtain the desired jet profiles. The characteristics of each individual pulse history will be described in detail in later chapters.

2.3   Wake Generator

A wake generator is placed 12.7 cm (0.53 Cx) upstream of the cascade inlet. A CAD model of the wake generator and its position in the tunnel can be seen in Figure 2-2.
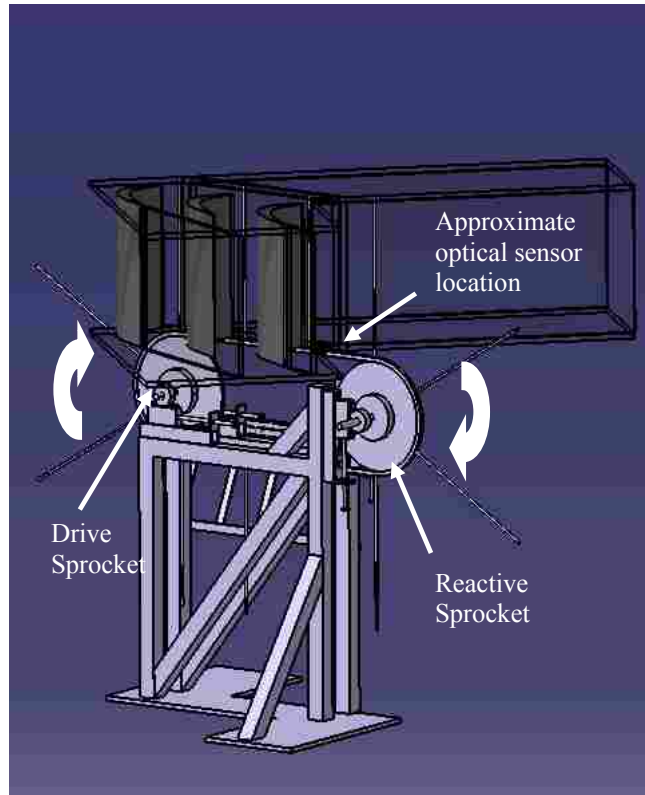
Figure 2-2: CAD model of wake generator and test section of tunnel.

Unsteady wake disturbances are created using 6 mm diameter carbon fiber rods. The rods are oriented in the spanwise direction and are drawn through the tunnel on a chain-sprocket system driven by a variable frequency motor. The sprockets are offset to ensure that the rods pass through the tunnel parallel to the leading edge of the turbine blades. Low density foam is used at both the tip and base of the rods to dampen vibrations and seal the tunnel. An optical sensor detects the passage of the rods as they exit the tunnel (see note in Figure 2-2) and sends a signal to the Parker-Hannifin pulse driver (when the wake generator is being used to phase-lock the data, t=0 is defined as the moment a rod passes through the optical sensor). This pulse driver controls a solenoid valve used to actuate the VGJs. The pulse driver is used to set the duration of the VGJ pulse and the

time of actuation relative to the input signal from the rod sensor. The speed of the rods was adjusted to maintain a normalized velocity near $U_{rod}/U_{in}=0.95$ (flow coefficient, $\varphi=0.85$) with a fluctuation of approximately ±2%. The period of the passing rods was measured to be 225 ms. Since the VGJs are synchronized to the rod passing frequency, this wake period yields a dimensionless forcing frequency of $F^+=0.27$ (for the synchronization study only). The rods are spaced at L/s=1.64, where L is the distance between the rods and s is the blade spacing. The larger spacing between rods (compared to the cascade spacing) is intended to simulate vane wakes impinging on a rotor blade row since the vane count is typically 60-75% of the blade count for a given LPT stage.

A variable frequency, permanent magnet, DC motor drives the chain-sprocket system. The ¼ hp, continuous duty cycle motor has a torque of 90 in·lb and a maximum rpm of 125. The ¾ inch motor drive shaft is fastened to the ¾ inch sprocket shaft by a coupler. The coupler allows for a slight misalignment of the shafts while still transferring the rotational energy to the chain-sprocket system. Figure 2-3 is a picture of the motor and drive sprocket.

Tensioners are placed on each side of the sprockets to tighten the chain and ensure that the shafts are aligned correctly. These tensioners have a fairly simple design consisting of a bracket, bolt, two washers, and two nuts (two other bolts are used to fasten the tensioner to the unistrut frame). Once the tensioners are bolted to the unistrut, the shaft mount bolts are loosened so that the shaft can slide along the unistrut. As the tensioner bolts are tightened, they push on the shaft mount tightening the chain. Once the desired tension has been reached the shaft mounts are re-bolted to the unistrut frame.
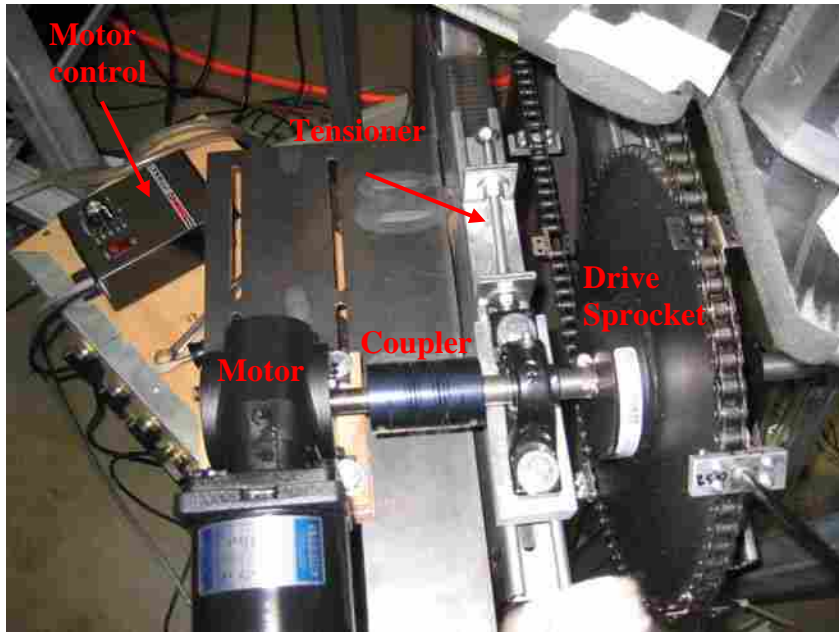
Figure 2-3: Wake generator motor and chain-sprocket system.
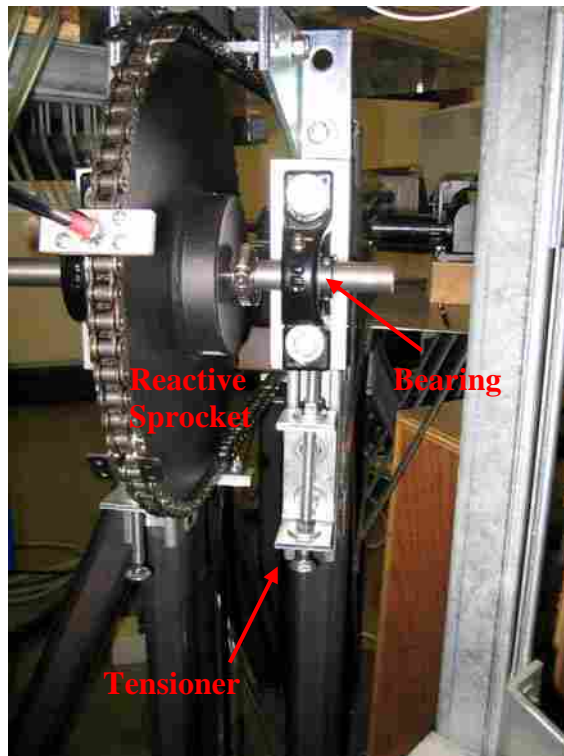
Figure 2-4: Tensioners of the reactive sprocket.

The sprocket shafts pass through pillow block bearings which are fastened to the shaft mounts. These bearings allow the shafts to rotate even with the added tension of the chain. A picture of the tensioners on the reactive sprocket is provided in Figure 2-4. The tensioners of the reactive sprocket are also used to offset the sprockets ensuring the rods pass through the tunnel parallel to the leading edge of the turbine blades. Figure 2-5 shows the tensioners used to move the drive sprocket.
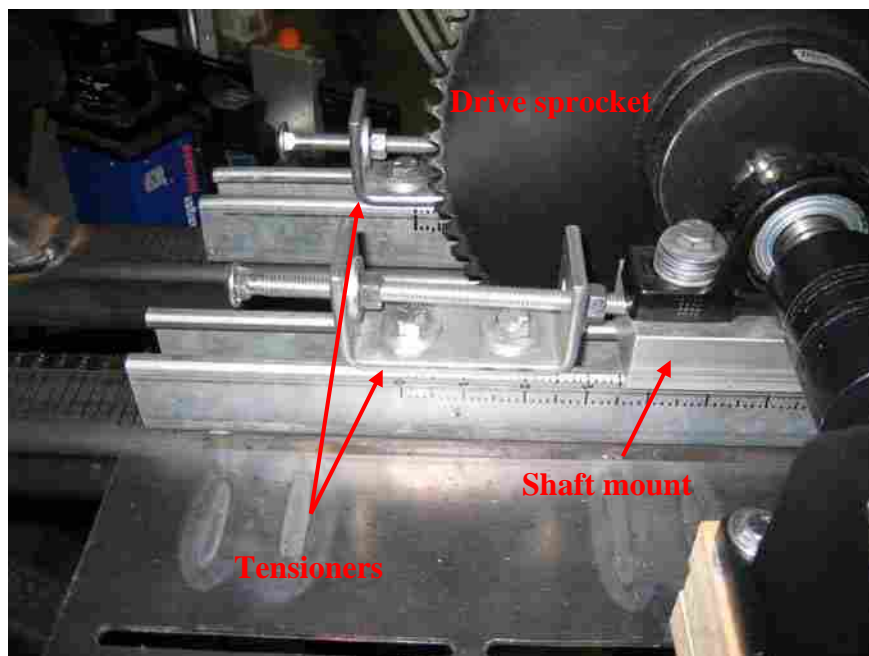
Figure 2-5: Tensioners of the drive sprocket.

2.4 Data Acquisition (PIV)

Data were taken using a LaVision PIV system mounted to a three axis traverse below the test section. A stereoscopic (3D) and three single camera (2D) sets of data were taken. The stereoscopic data were used to identify the three dimensional flow in the region of

the jet injection, while the single camera data sets were taken from the region of the VGJs to the trailing edge of the blade. A Nd:YAG laser was used to project two consecutive 1 mm thick laser sheets (with 250 μs time separation) in the x-y plane into the test section (see Figure 2-1 for the coordinate system). The flow was seeded with olive oil particles having diameters between 1 and 2 μm. Two high-speed digital cameras were positioned below the test section. The cameras have a resolution of 1376 by 1040 pixels. A picture of the PIV system (not in position to take data) can be found in Figure 2-6. A green caricature of the laser was added to the figure.
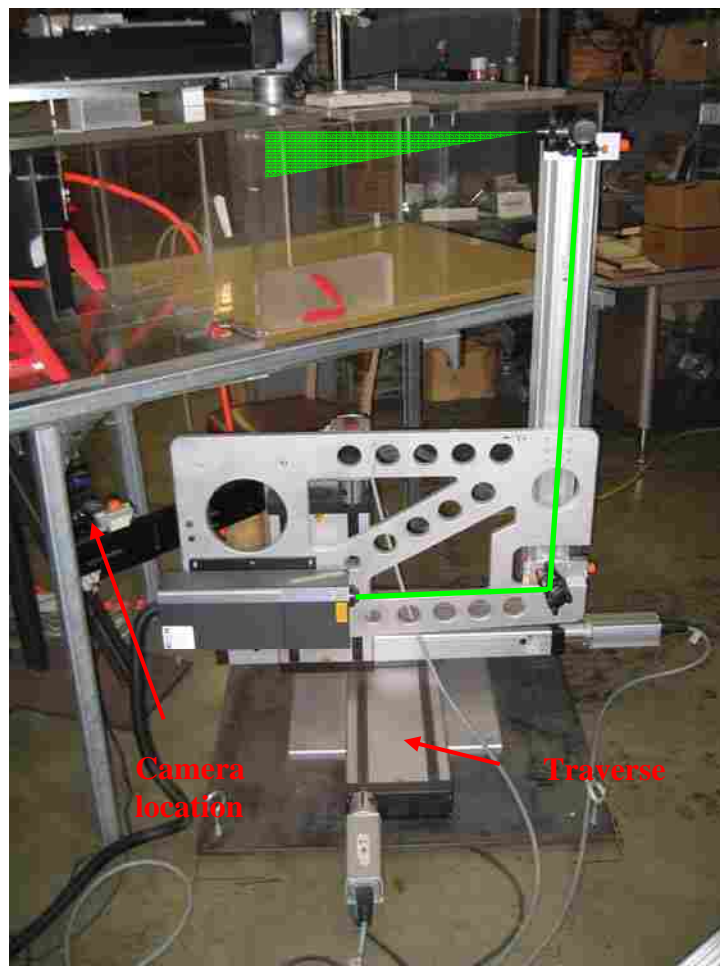
Figure 2-6: The PIV system (set up to take single camera data).

2.4.1 PIV Calibration

Although calibrating the PIV system seems like a trivial matter, it is actually a very difficult and important process. Although the process varies with every calibration, a general outline of the procedure is included below.

A pinhole calibration plate is placed in the tunnel. The plate is fastened to a stand that rests on the top of the tunnel. A picture of the calibration plate is found in Figure 2-7.

Figure 2-7: Calibration plate.

The plate is covered with dots that are all equally spaced (10 mm apart). The plate is not flat but has alternating high and low surfaces for each row of dots. The difference in surface thickness from peak to valley is ~1 mm. These alternating surfaces appear in the figure as white lines (the white lines are caused by the glare of the camera flash).

The plate is leveled using wooden wedges and heavy weights. The PIV cameras are then brought below the plate, using the traverse, and crudely focused. An option in

18

LaVision allows the user to view two camera images superimposed on each other. Using this option, each camera is aligned to the same position (in the stereoscopic calibration). In order to assist the person calibrating, there is a dot with crosshairs in the center of the plate. This dot is centered on the camera images. Once these dots are aligned in each of the camera images, the cameras are then finely focused. Focusing involves the use of the Scheimpflug, an optical correction which rotates the camera lens into the orientation of the calibration plate. Figure 2-8 contains depictions of the setup for the single camera and stereoscopic data sets.
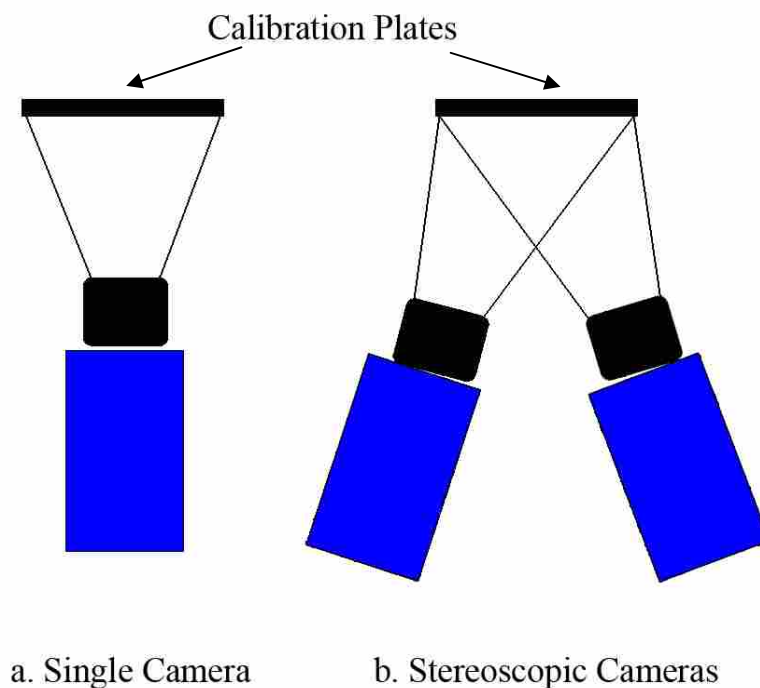
Figure 2-8: Depiction of camera setup for the single and stereoscopic data sets.

The left side of the image represents the single camera setup. The camera is located directly below the calibration plate so the Scheimpflug is not adjusted (lens is flat with

the camera body). The stereoscopic setup is depicted on the right side of the image. The stereoscopic cameras are offset from the calibration plate. LaVision suggests a maximum difference in angle between the two cameras of 30˚. Adjusting the Scheimpflug rotates the camera lens closer to the plane of the calibration plate. This allows the camera to be focused across the entire plate. Adjusting the Scheimpflug and focus is an iterative process.

The next step in the calibration process is ensuring that there is ample contrast between the white dots and black background of the plate. This is accomplished by placing a light source below the test section. Optimal lighting conditions are achieved when the contrast is greatest without saturating the image with light. Once this lighting condition has been found, the calibration routine in LaVision captures the plate images and creates the calibration. LaVision then calculates the uncertainty in pixel location which is used to predict the uncertainty in the PIV.

The calibration plate is subsequently used to position the laser in the focus plane of the cameras. The laser is set on low setting, and the optics are adjusted until the laser sheet is aligned with the bottom edge of the calibration plate. Laser thickness is also adjusted at this point. The laser sheet can not be too thick or too thin. If it is too thin, the seed particles may move in and out of the laser sheet prematurely. A thick laser sheet introduces error into the velocity predictions and reduces the spatial resolution. The optimal laser sheet thickness depends on the circumstances. In this study the laser sheet thickness was ~1 mm.

PIV depends on two lasers to create successive images of the same set of particles. The time required between the lasers depends on the velocity of the fluid. If the lasers are

not fired rapidly enough, two different sets of particles will be captured in the successive camera images making cross correlation impossible. If the time between lasers is too small, the particle displacement will not be sufficient. This will increase the error in the velocity predictions drastically. LaVision suggests a particle displacement near 8 pixels.

The calibrated PIV system is then used to determine the amount of particle seed needed to take data. Images are taken and processed with varying amounts of seed until the stray velocity vectors of the resultant velocity field are eliminated. The flow is seeded upstream of the test section. The seeder (found in Figure 2-9) is attached to a high-pressure air line (the red hose). It has a regulator that controls the amount of particles that

Figure 2-9: PIV particle seeder.

are introduced into the tunnel. The seeder operates by introducing a high speed jet of air into a reservoir of oil. The jet causes the oil to atomize, which then flows into the wind tunnel through a tube (clear, vertical tube on the right side of the figure).

Glare is also an important consideration when taking PIV data. Glare is very difficult to eliminate completely, especially on a curved surface like the Pack B turbine blade. The initial PIV data had a considerable amount of glare. In order to eliminate a large portion of this glare, the acrylic, inner turbine blade was painted flat black. The paint effectively absorbed much of the glare. The remainder of the glare was minimized by adjusting the intensity of the laser. This was done while maintaining sufficient intensity to illuminate the seed particles.

2.4.2   Single Camera PIV Data (2D)

Single camera measurements were taken in 18 spanwise (z) locations for three different VGJ/wake configurations. The z locations were 1.5 mm apart and spanned one VGJ hole pitch. The first z location was taken directly below a midspan VGJ where the flow was shown to be spanwise uniform. Subsequent levels were taken by traversing toward the top of the test section in the negative z direction according to the right hand rule (x is the flow direction and y is normal to the blade surface). The single camera data set required two different test windows to capture flow along the entire blade. These windows covered an upstream (~50% to ~81% Cx) and a downstream (~80% to ~100% Cx) portion of the blade with approximately 6 mm of overlap (see Figure 2-10).

The location of each window was identified using a cardboard template that fit the blade profile. The template is labeled with the axial chord locations. The PIV cameras and template were used to identify the extent and location of the upstream and downstream test windows. The template was also used to measure the overlap between the windows.
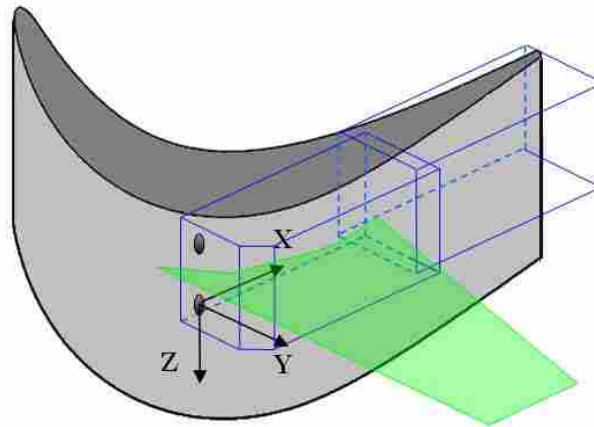
Figure 2-10: Upstream/downstream data collection regions (only part of the total blade span is depicted). The green plane is a representation of the laser sheet.

The data windows were later merged together to create a continuous set of data as depicted in Figure 2-11. A weighted averaging technique was employed in the region of overlap. It should be noted that all the data (both PIV and hot-film) are presented in the
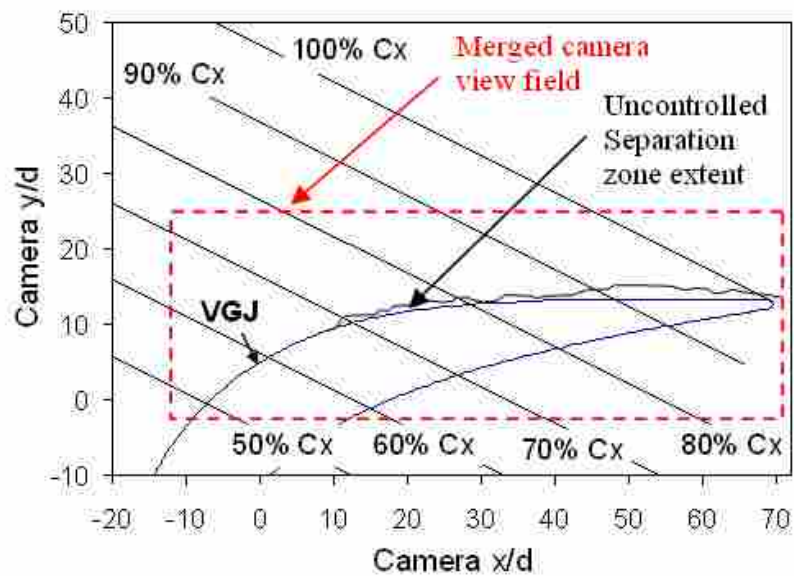
Figure 2-11: The coordinate system used to present the data. Also included are the merged camera view fields, the axial chord lines of the Pack B, and a representation of the separation bubble.

camera coordinate system. In the region of interest (59% to 100% axial chord) the blade is relatively flat. The result is that the x and y coordinates of the camera are approximately streamwise and surface normal in this region (although not exactly).

2.4.3   Stereoscopic PIV Data (3D)

Only one data window was used for the stereoscopic PIV data. This data window was carefully positioned to maximize the visibility of the jet influence from its inception to the upstream end of the separation bubble. This resulted in a much more detailed set of data. This window ranges from C_x of 59% to ~85%. In contrast to the single camera data, this data set covers 26 z elevations spanning one VGJ hole pitch (1 mm increments). The fundamental purpose of taking the stereoscopic data was to increase the spatial resolution with the intent of isolating the vortical structure induced by the VGJ. The data were acquired at 12 intervals (focused in the region of the pulse) during the VGJ pulsing period.

2.4.4   Particle Image Velocimetry Post Processing

At each location, window and data collection interval, 40 images were taken, processed and averaged. It was previously shown that averaging with more than 40 images made no notable difference in the average velocity field results[18]. A blade mask was created prior to processing the images to eliminate the blade surface from the region of interest. This mask eliminated any light intensity in the blade region, thereby assigning the velocity vectors in the region to zero. An example of a seed image with and without a blade mask is presented in Figure 2-12.
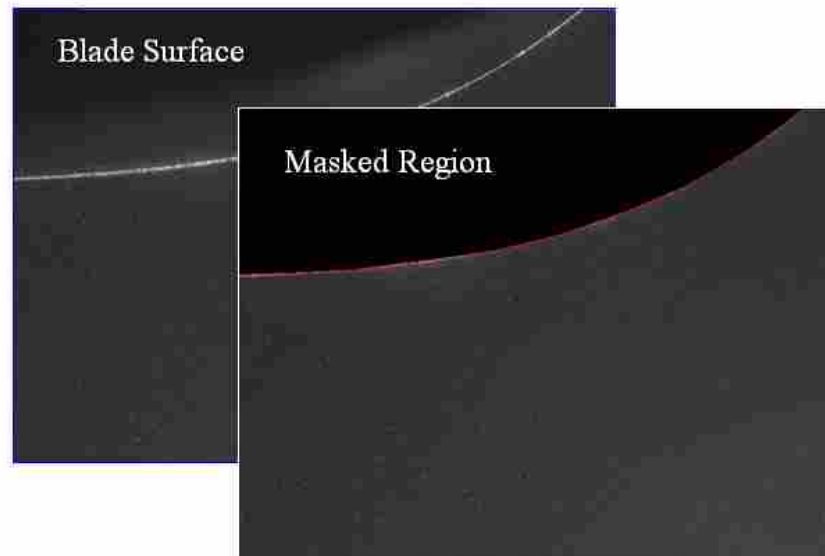
Figure 2-12: Seed image with and without a mask.

Vector processing was initially performed with 64 x 64 pixel interrogation windows. The interrogation windows were then refined to 32 x 32 pixels. LaVision's standard fast Fourier transform (FFT) correlation and a 50% overlap were used for each interrogation window size during vector processing. Any velocity vectors greater than 3.5 m/s were immediately eliminated given that the maximum velocities were expected to be below 3.3 m/s.

The resultant velocity vector fields were loaded into Matlab. The velocity fields were smoothed using a top hat filter to eliminate higher-order spatial variations. The resulting 3D blocks of data provide u and v velocity data for the single camera data sets and all 3 components of velocity for the stereoscopic data. These data were also used to create vorticity fields. The Matlab program allowed for figures to be created from the data in all three planes (stereoscopic data).

According to LaVision[19] the uncertainty in the seed particle displacement is approximately 0.2 pixels. This translates to a velocity uncertainty of ±0.08 m/s (see Appendix: Uncertainty Analysis).

2.5 Hot-film Data

Phase-locked hot-film data were collected to substantiate the results obtained through particle image velocimetry. These data sets were collected using a hot-film mounted to a blade-following ("follower") device. A picture of the blade follower is found in Figure 2-13.
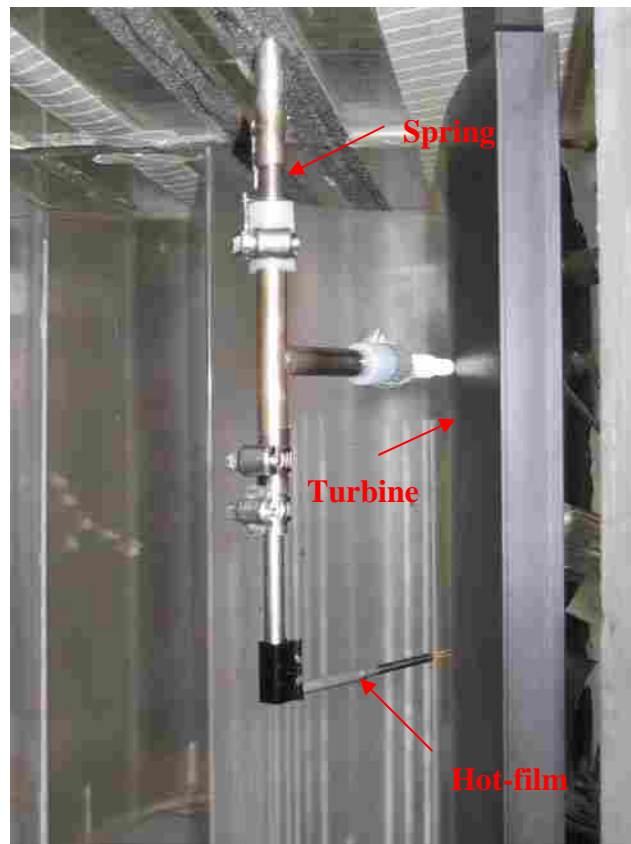
Figure 2-13: Blade follower device.

The picture is taken from a position downstream of the cascade. The black object that spans the picture vertically is the turbine blade. The hot-film anemometer used in this study had a diameter of 50.8 μm, a length of 1.02 mm, and a frequency response of approximately 200 kHz. The follower was fastened to a 3-axis traverse that sat on top of the test section. As the traverse moved in a linear direction, the spring loaded follower maintained the hot-film at a constant distance from the turbine blade wall.

Data were collected along the blade from ~48% C_x to ~96% C_x. Sixteen profiles were taken with wall-normal distances ranging from 1.2 mm to 20 mm. These profiles were taken at z/d=6. This location was chosen because the VGJ causes the greatest impact on the separation zone in this region. Each blade profile consisted of 64 data locations. These data locations were not equally spaced across the blade but were more concentrated in the region of the separation zone. Twenty four seconds of data were collected at each location with a sampling frequency of 10 kHz. This resulted in 240,000 total data points (at each location). U_{rms} and intermittency were calculated from these data and are used throughout this thesis. The methodology for the estimate of the intermittency is described in detail in Bons et al.[20] The hot-film had an uncertainty of ±0.03 m/s (see Appendix: Uncertainty Analysis).

The hot-film was calibrated in the wind tunnel using a pitot static tube connected to a Druck differential pressure transducer. The tunnel was used for calibration (rather than a free jet) because the wind tunnel temperature can be adjusted, allowing a calibration that accounts for temperature. The calibration was performed at normal operating conditions (70˚F) and while the cooler (50˚F) was operating with a range of velocities from 0.8 m/s to 8 m/s.

3   The Mechanisms of Control

This chapter explores the important characteristics of the VGJ pulse histories, focusing primarily on the effects of the initial actuation, the pulse duration, and the relaxation time between pulses. The mechanisms of control responsible for boundary layer reattachment are also investigated.

3.1   Pulse Histories

Two distinct VGJ pulse histories were created. Each pulse history was carefully selected to isolate the effects of the VGJ actuation and relaxation time. These pulse histories are depicted in Figure 3-1. The first pulse history had a frequency of 5 Hz (period of 200 ms, T_{5Hz}=200 ms), a blowing ratio of 2, and a duty cycle of 25%. The second pulse history had a frequency of 3 Hz (period of 333 ms, T_{5Hz}=333 ms), a blowing ratio of 2, and a duty cycle of 5%. Also included in the figure are the time locations of data acquisition for the PIV data. The blue triangles represent the 8 time locations for the 5 Hz signal, and the red squares represent the 9 time locations for the 3 Hz signal.

In order to isolate the important characteristics of the VGJ pulse history, data were collected for both signals at the same time relative to the initial VGJ actuation and recession. This was done so that direct comparisons of the separation bubbles could be made relative to these events.
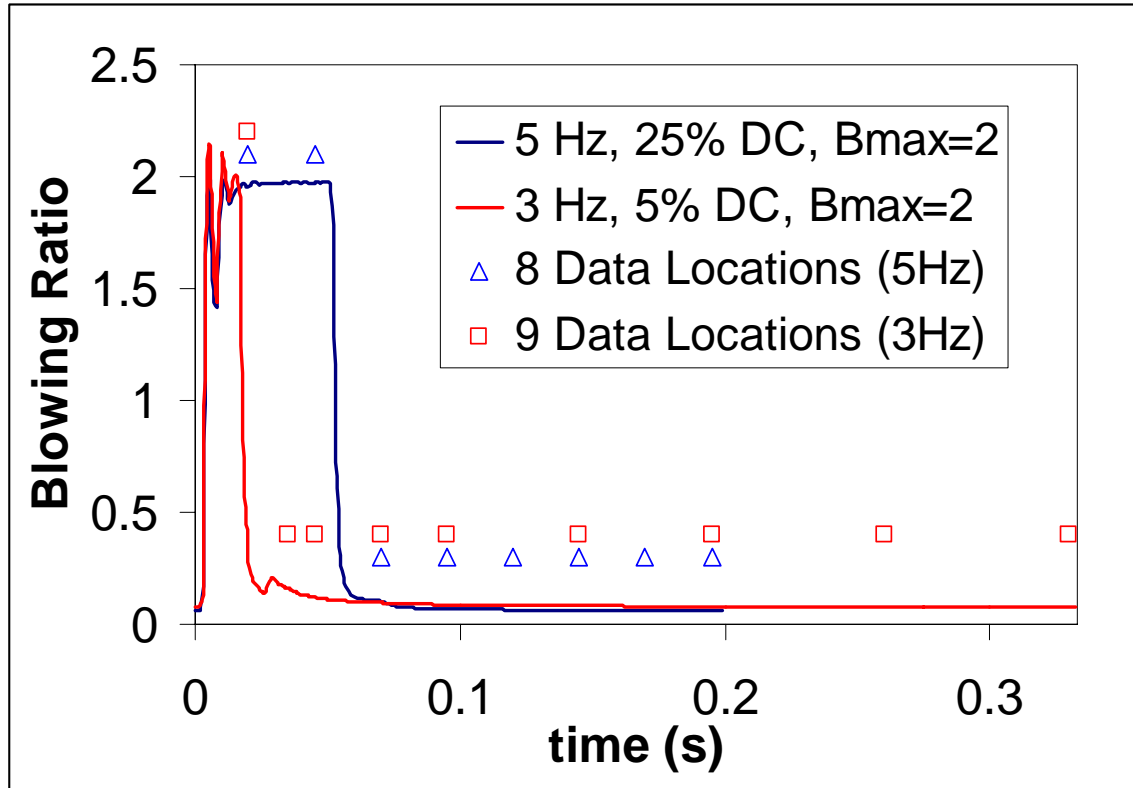
Figure 3-1: VGJ Pulse Histories and Data Acquisition Locations (in time)

3.2   Time-Averaged Cp Distributions

The time-averaged effect of pulsed VGJs on the Pack B separation bubble is evident in the Cp distributions presented in Figure 3-2 (the VGJs are located near 59% C_x). The VBI calculation is included as a benchmark for non-separating flow. The VBI is represented by a solid blue line in the figure. Also included is a lower Re number (50K) estimate of the Cp distribution predicted by the MISES code (solid black line). MISES predicts a separation near 75% C_x as shown in the figure. This separation region reattaches to the blade near 87% Cx. Cp distributions that closely resemble the VBI are considered to be attached, while deviations from the VBI are indicative of boundary layer separation. The uncertainty in Cp was ±0.11 (see Appendix: Uncertainty Analysis).

30
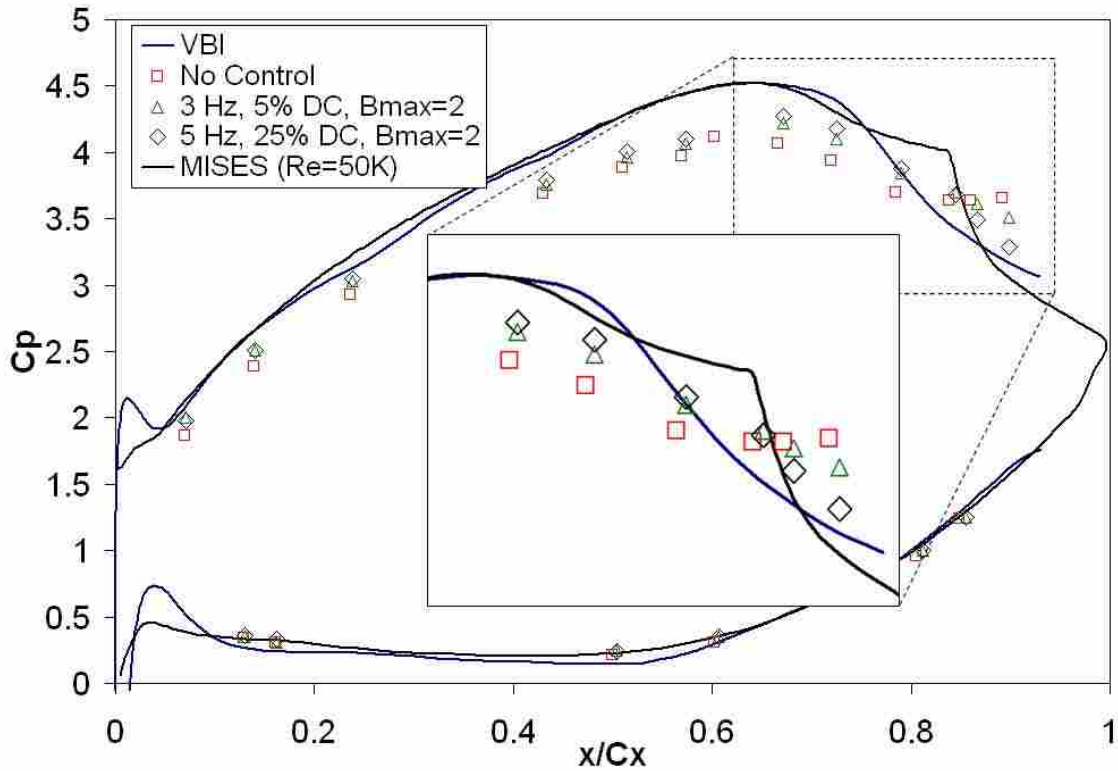
Figure 3-2: Cp distribution on the Pack B profile.

The no control (no VGJs) Cp distribution, which is represented by the red squares, suggests massive separation without re-attachment in the region of the pressure taps. This separation region is evidenced by the departure from the shape of the VBI near 80% C_x. After departure, the no control distribution remains flat while the VBI and MISES predictions decrease in Cp. The 5 Hz distribution more closely resembles the VBI and MISES predictions. A slight deviation is evident from ~80% to ~90% Cx. This measured separation region is much smaller than the MISES prediction. The 3 Hz distribution lies between the no control and 5 Hz distributions. This plot suggests that pulsed VGJs offer effective time-averaged control of the separation region, with the 5 Hz pulse history

31

inducing more control than the 3 Hz. This difference in control extent will be further explored using PIV.

3.3   5 Hz Pulse History Results (PIV)

Figure 3-3 presents three-dimensional iso-velocity surfaces of U/U_{in}=1.0 taken from the 5 Hz PIV data. The data are normalized by the cascade inlet velocity U_{in} (U_{in}=1.54 m/s). These surfaces were constructed by traversing into the 3D PIV data block in the negative y direction starting from the freestream. At each x and z location the first occurrence of the velocity surface was recorded. The blade profile was then removed from the resultant surface to aid in visualization. As a result the vertical axes of the plots are approximately the wall normal distances. The lower velocity region characteristic of a separation bubble was identified with these surfaces and can be seen in the contour plots as elevated regions in the flow. The colors of the velocity surface represent the blade wall distance. The plots are presented with the flow moving from right to left at the indicated x/d locations of the camera domain. The jet enters the velocity surface at a z/d of approximately 9 (VGJ hole center). The red arrows found in t/T_{5Hz} of 0.10 and 0.23 of the figure are an approximate representation of the jet hole location (not orientation). An iso-velocity surface of the no control data is also included in the figure as a reference.

Surface plots of the 5Hz data show the separation bubble is at its maximum size during t/T_{5Hz}=0.10 of the VGJ jet cycle. It should be noted that at this point the jets have not been on long enough to impact the bubble. At t/T_{5Hz}=0.23 the effect of the jets on the separation bubble is evident as seen by the saw-toothed shape at the upstream end of the separation bubble. At this point the iso-velocity surface (representing the separation

32
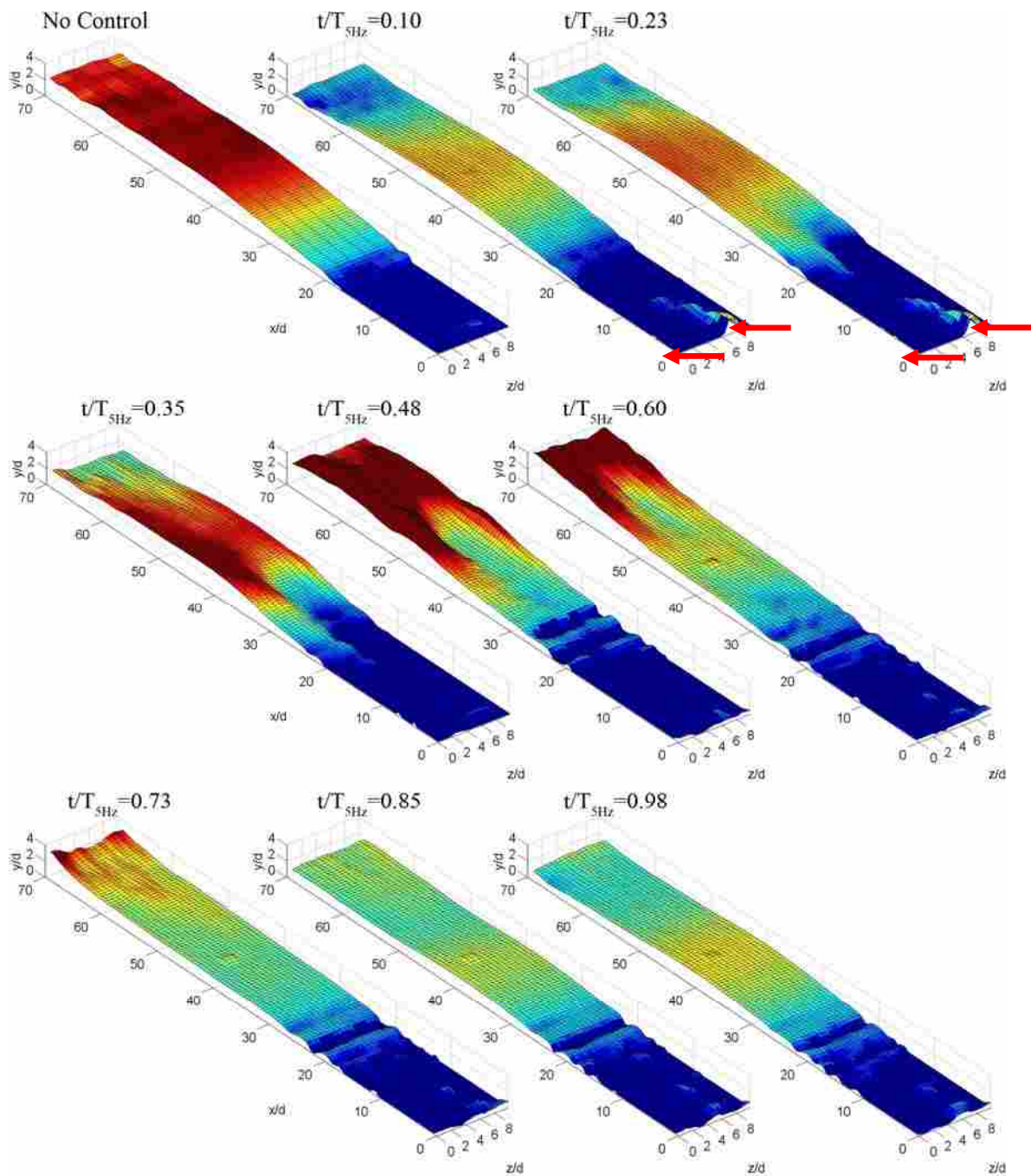
Figure 3-3: Phase-locked iso-velocity surfaces of U/U$_{in}$=1.0 created from the 5Hz PIV data. The no control results are also included. Red arrows indicate the approximate jet location.

bubble) also begins to bunch up between x/d=40 and x/d=60. By t/T_{5Hz}=0.35 the two-dimensional downstream effect of the jets begins to take shape. The jets have succeeded in reattaching a portion of the upstream end of the separation bubble, and the saw-tooth shape has moved further downstream. The maximum wall distance of the iso-velocity surface has again increased, denoting a bunching up of the separation bubble. A more-rounded separation bubble begins to take shape by t/T_{5Hz}=0.48 as the initial 3D jet disturbance evolves into primarily a 2D flow feature which is ejected from the blade. By t/T_{5Hz}=0.60 the saw-tooth shape has disappeared and the 2D disturbance begins to move off the blade leaving behind a significantly reduced iso-velocity surface (separation region). The separation bubble slowly recovers from t/T_{5Hz}=0.73 until it is again impacted by the subsequent VGJ disturbance. The observant reader will notice a small elevated dimple near x/d=40 from t/T_{5Hz} of 0.60 to 0.98. This corresponds to a region of moderate glare in the PIV images and is not credited to the fluid flow. Also, the wave-like structures seen in the upstream end of the separation bubble from t/T_{5Hz} of 0.48 to 0.98 are a result of the blade masking technique.

The 2D bunching of the fluid in the separation zone seen in Figure 3-3 can be attributed to the increased velocity of the reattached flow region. As the flow reattaches, the higher momentum fluid moves down to the wall where it meets the low momentum fluid in the separation zone. The energy of the high momentum fluid is reduced as it mixes with the low-momentum fluid. This results in a bunching of the separation zone made manifest in the iso-velocity surfaces as an elevated 2D bulge. This 2D bulge takes shape because the downstream end of the separation region convects at a lower mean streamwise velocity. The net result is that the discrete (3D) jet disturbances are

transformed into a spanwise uniform (2D) wavelike disturbance that is pushed off the blade by the reattached high momentum fluid.

3.4   Transition Line Theory

To further explore the jet-bubble interaction, stereoscopic PIV data were used. As was stated earlier, the stereoscopic data have a much higher spatial resolution and therefore are more detailed in the region of the VGJ.   It should be noted that the stereoscopic data were collected using a similar pulse history to the 5 Hz data. The inlet
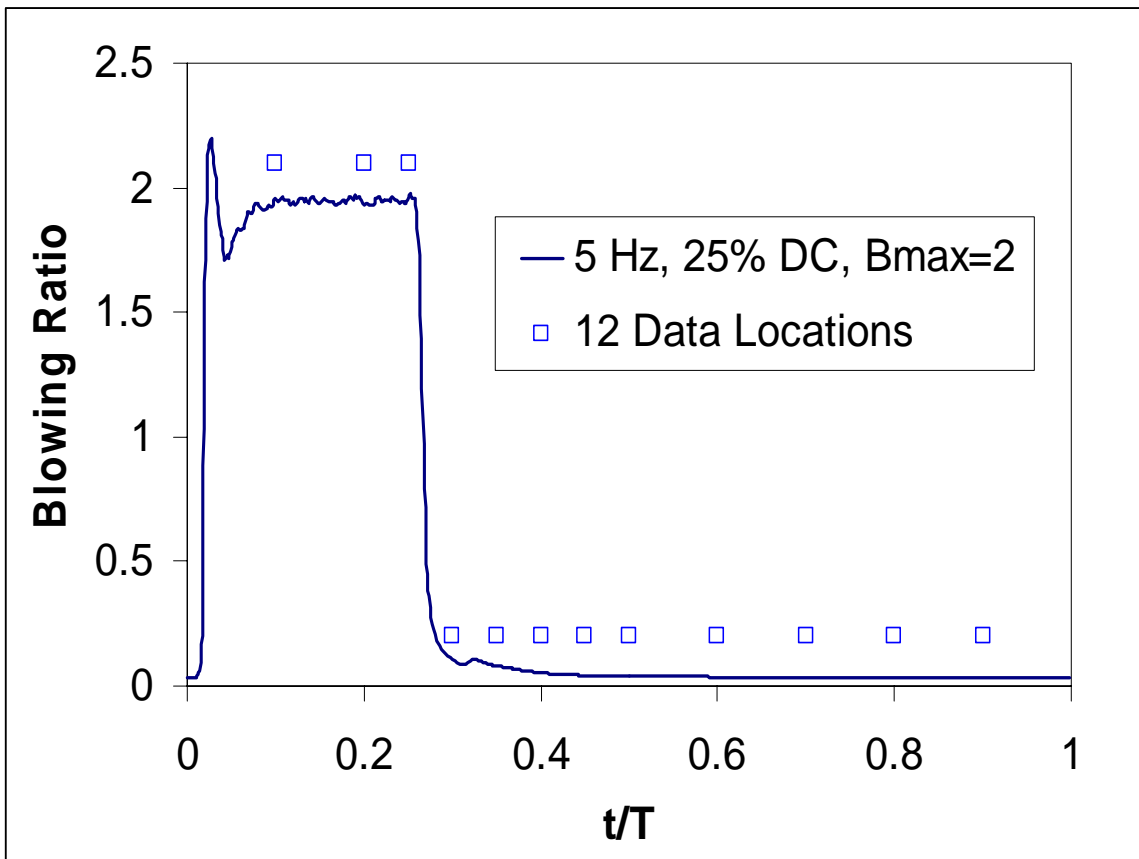
Figure 3-4: Stereoscopic VGJ pulse history. Data acquisition locations are also included.

conditions of the wind tunnel were likewise similar to the 5 Hz data. The stereoscopic pulse history and the twelve time locations of data acquisition are provided in Figure 3-4.

The PIV data domain was traversed in the streamwise direction at a fixed 1.0 mm offset from the blade profile. The offset was taken along the y axis of the camera frame thus it is only approximately the true wall normal distance. The result is a contour map of u/U_{in} that clearly shows the jet migration in both the x/d and z/d directions at an offset of 1.0 mm. Two of these contour plots are provided in Figure 3-5.
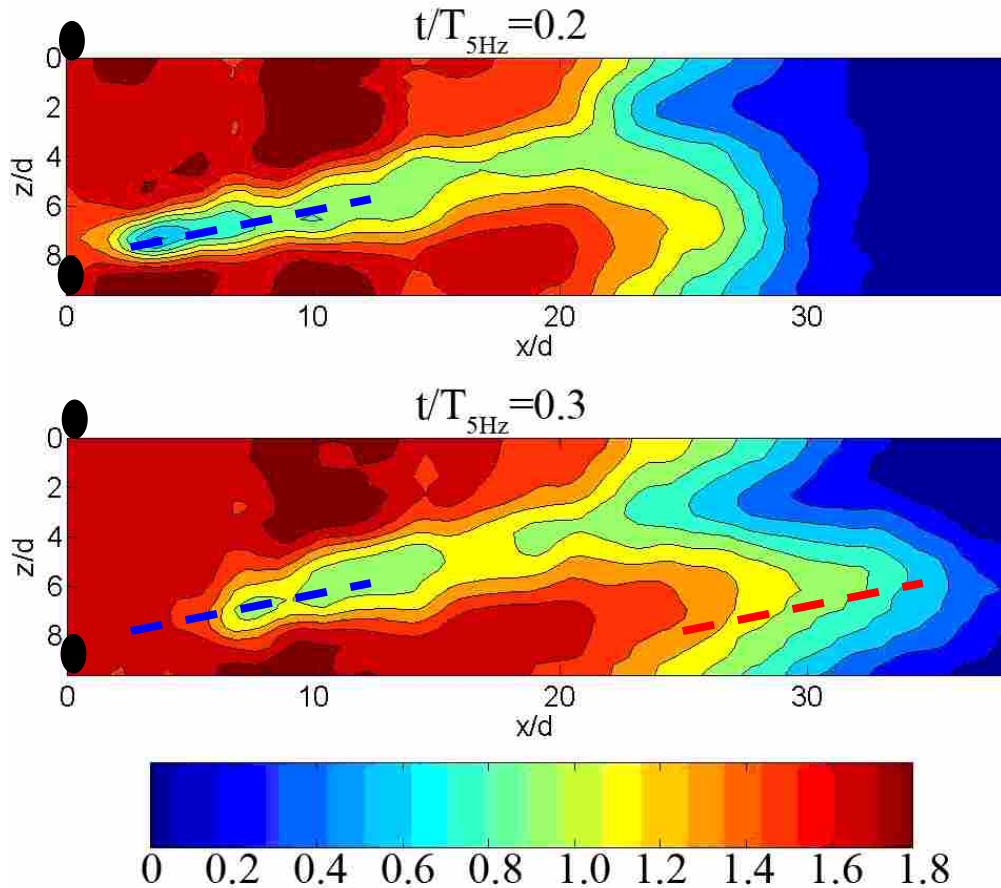
Figure 3-5: u/U_{in} velocity contours at a wall offset of 1 mm (looking toward the blade surface). The jet locations are represented on the left side of the images as black ovals.

36

The wall offset of 1.0 mm was chosen because it clearly depicts the path of the jet fluid. The line of influence created by the jet is denoted by a dashed blue line on the left side of each of the diagrams in the figure. The jet fluid is injected with zero streamwise momentum and must be entrained by the flow. Consequently, the jet trajectory is characterized by a region of low u/U_{in}. The line of influence created by the jet acts as a trigger for boundary layer transition. The downstream effect of this transition line can be seen at the upstream end of the separation region in the plot of t/T_{5Hz}=0.3. In the plot of t/T_{5Hz}=0.3 the VGJ has been deactivated, causing the upstream end of the jet influence to propagate downstream. The saw-tooth shape seen in the separation bubble (denoted with a dashed, red line) approximately parallels the orientation of the upstream transition line created by the jet. The streamwise penetration seen in the separation zone suggests that the location of the transition plays an important role in the control.

Experimental data collected with a single-element hot-film on the same Pack B test section supports the transition line theory presented above. Figure 3-6 shows the intermittency calculated with the hot-film data at t/T_{5Hz} of 0.15, 0.27, 0.48, and 0.69 at a z/d of 6.

The separation bubble is represented by the red region at the far right of the plots. An intermittency of unity (red regions) connotes fully turbulent flow while an intermittency of zero (blue regions) connotes laminar flow. Separated boundary layers are inherently unsteady due to the removal of the wall influence. This unsteadiness causes the flow to transition and the intermittency trigger indicates turbulence. The VGJs (represented by a red arrow) are positioned at 59% C_x. The VGJs are active at t/T_{5Hz} of 0.15 and have just been deactivated prior to the plot of t/T_{5Hz}=0.27. The plots show that when the VGJs are
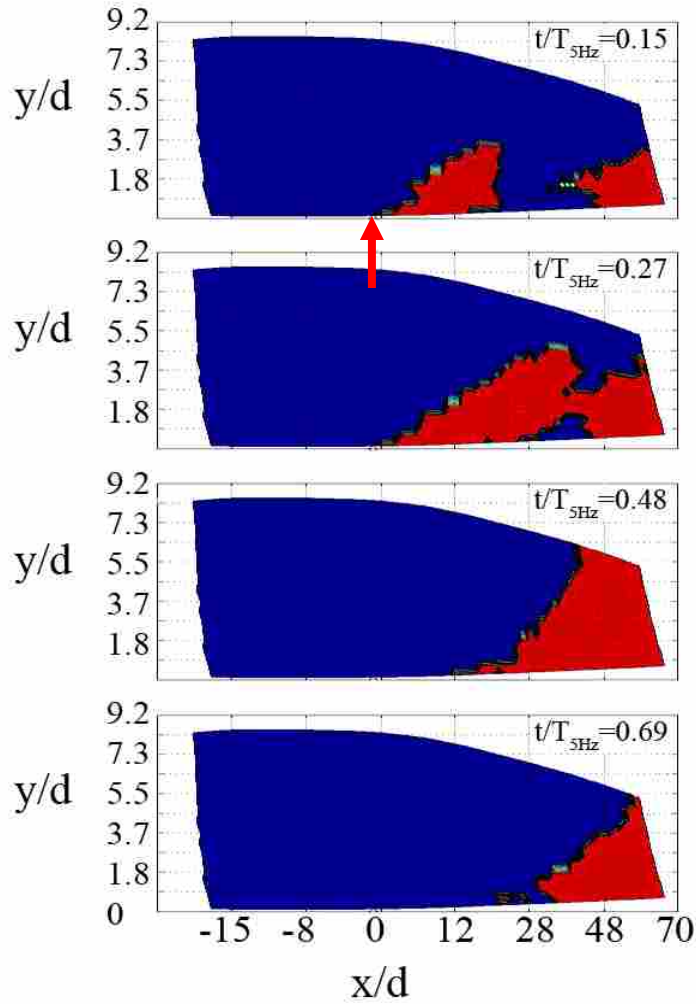
Figure 3-6: Intermittency contour plot taken from hot-film data at z/d=6. An intermittency of 1 indicates turbulent flow, 0 indicates laminar flow.

active the flow transitions to turbulent. This is represented by the red region spanning ~59% C_x to ~75% C_x in the plot of t/T_{5Hz}=0.15. This region of transitioned flow propagates downstream by t/T_{5Hz}=0.27 and begins to interact with the separation region. Once the VGJs are deactivated the jet-induced transitioned region quickly moves downstream. The subsequent plots depict a bunching of the separation zone (t/T_{5Hz}=0.48) which is then pushed off the blade leaving primarily attached flow behind. The complete data set can be found in Reimann et al.[21]

3.5   3 Hz Pulse History Results (PIV)

Patterns similar to the 5 Hz data set are found in the 3 Hz data presented as iso-velocity surfaces in Figure 3-7. A comparison of the iso-velocity surfaces for t/T_{5Hz}=0.10 (Figure 3-3) and t/T_{3Hz}=0.06 (Figure 3-7) shows a larger development (~30%) of the separation bubble in the 3Hz data. A slight impact of the jet disturbance on the separation region is visible in the upstream end of the separation bubble at t/T_{3Hz}=0.11. The formation of the saw-tooth shape isn't visible until t/T_{3Hz}=0.21. Promptly the three dimensional influence of the jet evolves into a 2D disturbance (by t/T_{3Hz}=0.29).

The overall effects of the VGJ-induced disturbances (5 Hz and 3 Hz) are very similar. In both cases the VGJs create three dimensional disturbances which later evolve in to 2D disturbances. These disturbances propagate down the blade reattaching the boundary layer. There are also some very obvious discrepancies, most notably the rapid evolvement of the three dimensional disturbance into a two dimensional disturbance in the 3 Hz data and the larger residual separation bubble of the 3 Hz data.

3.5.1   Pulse Duration

Previous work by Bons et al.[10] with the Pack B blade profile suggested that the major source of VGJ separation control was the starting event of the pulse. The plots of t/T_{3Hz}=0.14 of the 3 Hz data and t/T_{5Hz}=0.23 of the 5 Hz data were taken at the same time relative to the initial event of the VGJ pulse. These plots are included in Figure 3-8.

A comparison of these iso-velocity plots shows that the 5Hz signal has created a much larger disturbance in the upstream end of the separation bubble. In the 5 Hz plot the upstream end of the separation bubble has begun to reattach and the saw-tooth shape is
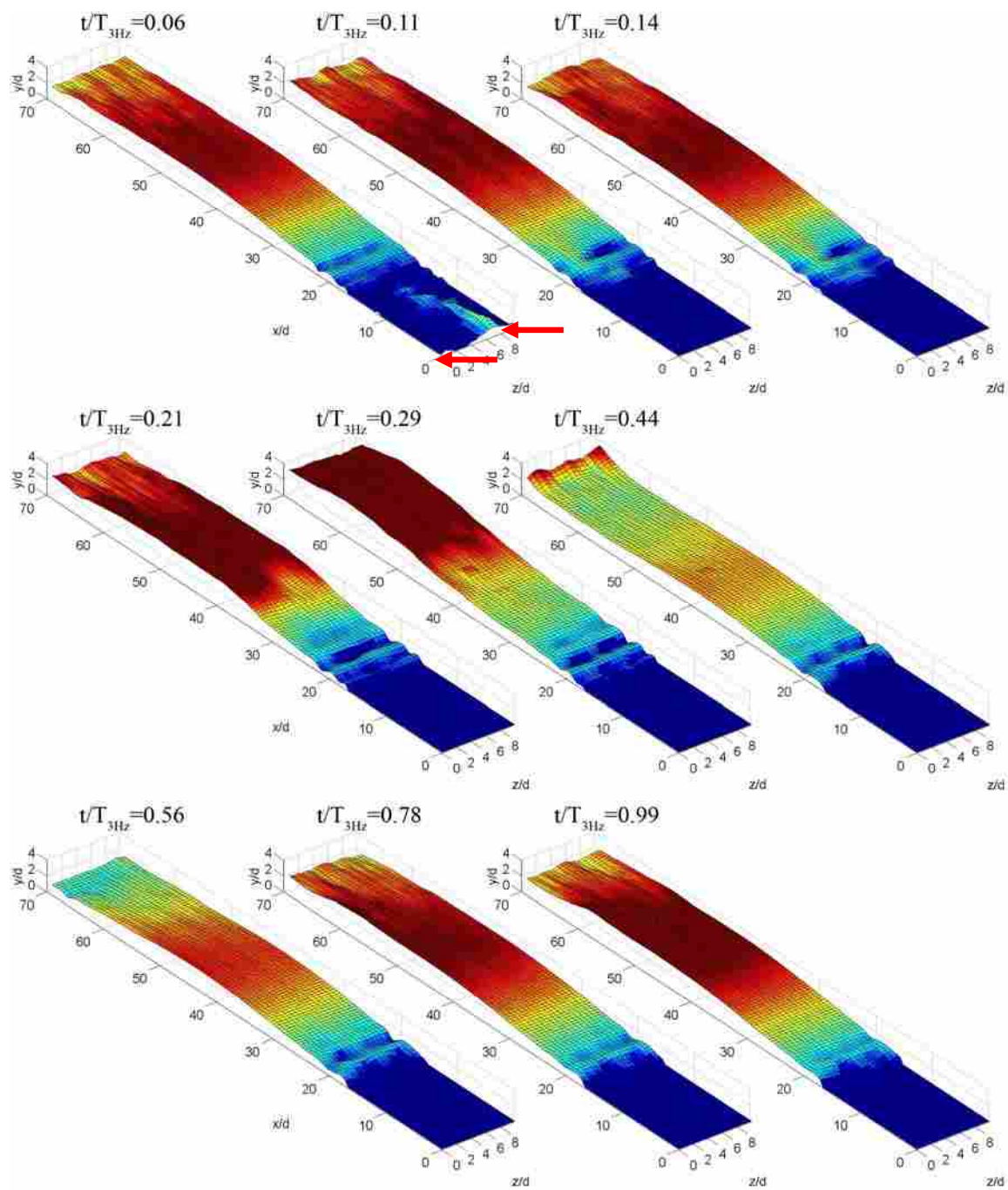
Figure 3-7: Phase-locked iso-velocity surfaces (u/U$_{in}$=1.0) for 3 Hz pulse history. Red arrow indicates approximate jet location.
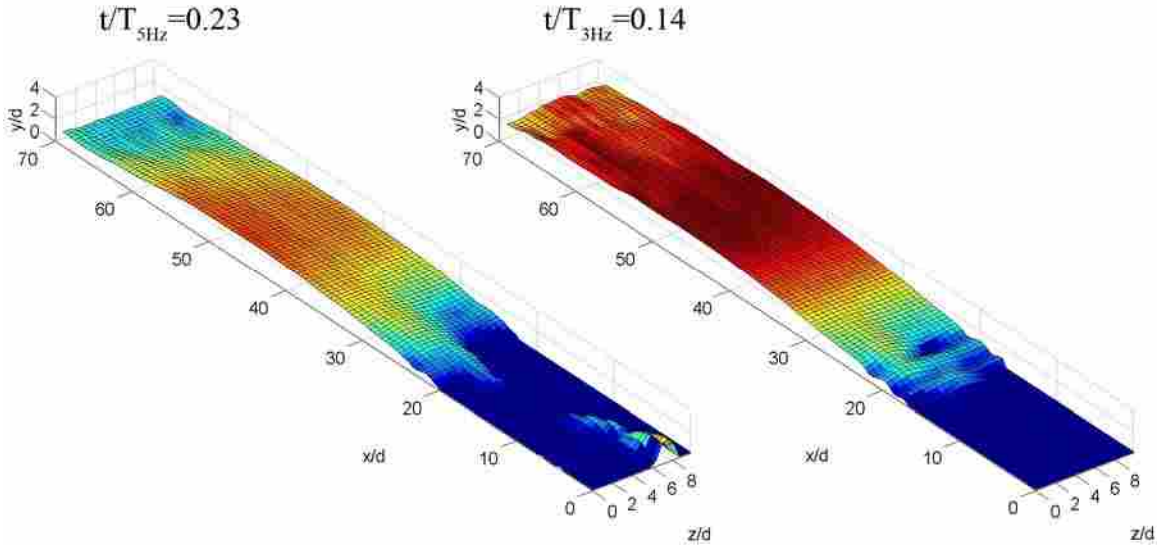
Figure 3-8: A comparison of the influence of the 5Hz and 3Hz jet pulses.

clearly visible. In comparison, the influence of the VGJ disturbance on the upstream end of the separation bubble in the 3 Hz data is barely visible. The present data suggests that the pulse duration may also play a significant role in the control, a logical conjecture considering that a longer pulse sustains the upstream transition[20].

The conventional model for separated flow transition suggests that transition starts in the separated shear layer and then convects down to the wall. Thus, propagation of the transition into the separation bubble is time dependent. The larger residual separation bubble visible in the 3 Hz data suggests that the jet-induced transition wasn't sustained long enough to propagate completely through the bubble. The reenergized portion of the separated flow grows into the 2D wave and is subsequently ejected as it was in the 5 Hz case. The remainder of the separation bubble regroups to its original size. In contrast, the 5 Hz control signal sustains upstream transition for a longer period of time, and as a result, the transitioned flow is able to propagate more completely into the separated regime ejecting a greater percentage of the separation bubble.

41

3.5.2 Relaxation Time

The differences in the extent of the control achieved by the two distinct VGJ pulse histories are also likely due to the maximum extent of the bubble (smaller in the 5Hz case). The relaxation time between the VGJ pulses is 150 ms for the 5 Hz data and 318 ms for the 3 Hz data. As a result the 3Hz signal allows the separation bubble to fully recover between jet disturbances, creating a ~30% larger separation bubble. Consequently, the jet-induced disturbance is not as effective at eliminating the separation region in the 3 Hz data.

In order to quantify the size of the separation bubbles at each time of data acquisition, each iso-velocity surface from Figure 3-3 and Figure 3-7 was averaged in the spanwise direction. The resultant average iso-velocity surfaces were then integrated and normalized by the no control averaged iso-velocity surface. Figure 3-9 is a plot of this integrated measurement for each of the time locations of data acquisition.

Figure 3-9 shows that the 5 Hz VGJ pulse history maintains the separation bubble at a reduced size for the extent of the period. The maximum reduction of the separation zone by the 5 Hz signal occurs at 170 ms. At this point the residual separation zone is ~59% of the no control separation zone. By comparison, the maximum extent of the control achieved by the 3 Hz signal is ~73% of the no control separation size.

The perceptive reader will notice that the final integrated iso-velocity surface for the 3 Hz (t/T_{3Hz}=0.99) data in Figure 3-9 is actually larger (~4%) than the initial integrated iso-velocity surface (t/T_{3Hz}=0.06). In theory these points should approximately coincide given that the separation bubble has not had any external influences. Although the discrepancy can not be fully explained, the author believes the trends presented in the
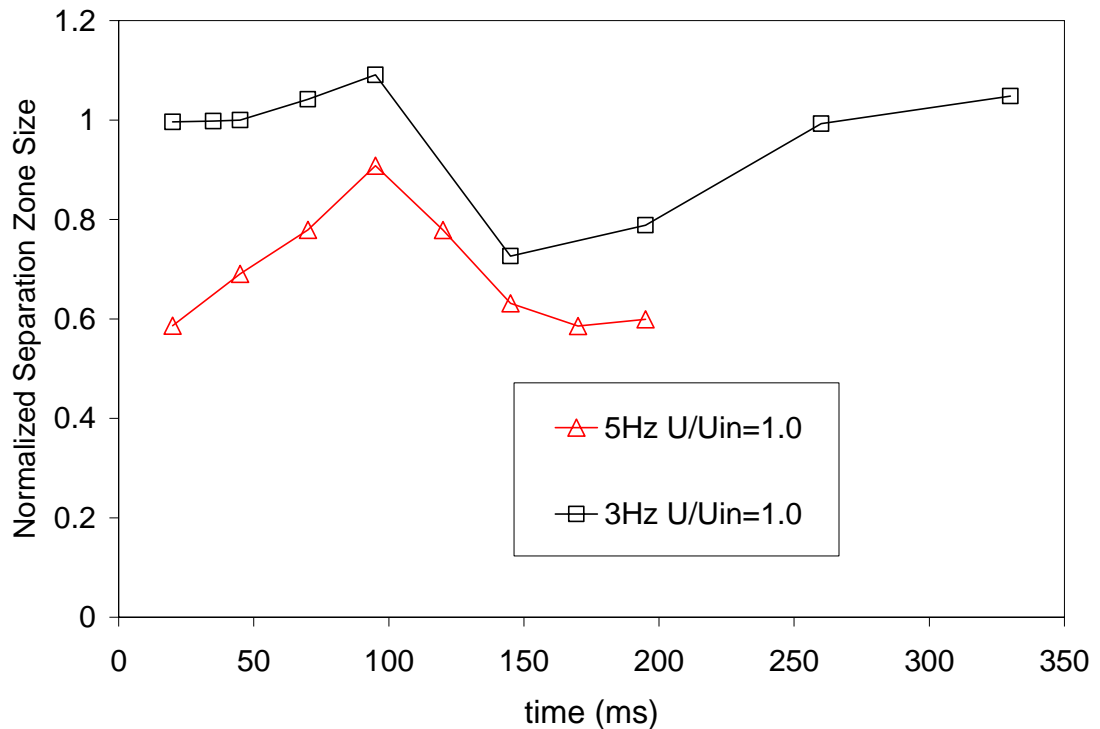
Figure 3-9: Integrated iso-velocity surfaces for the 3Hz and 5Hz data.

figure are accurate. The discrepancy may be attributed to a slight change in the inlet conditions, or, more likely, slight fluctuations in the optics for the laser sheet.

3.6   The VGJ-Induced Vortical Structure

To this point, the three-dimensional nature of the jet's unsteady effect on the separation bubble has been attributed primarily to a VGJ-induced transition of the boundary layer. This conclusion is supported in the literature[9,21]. The stereoscopic PIV data were used to clarify the role of vortical structures in the VGJ control. The stereoscopic data were taken with the same pulse history used to collect the single camera 5 Hz data. This pulse history was chosen because the VGJs remain active longer than the 3 Hz data. It was believed

that the VGJ induced vortical structure would be most evident with a longer jet duration. Figure 3-10 contains streamwise vorticity data (y-z plane) at two different time locations relative to the jet (5 ms before the VGJ turns off and 5 ms after it turns off).

In this study, the blowing ratio of the VGJ was $B_{max}=2$, the jet duration was 50 ms, and the duty cycle was 25%. The streamwise vorticity for four x/d locations is provided in the figure allowing side by side comparisons of the data for both time locations. The left column is the data taken 5 ms before the VGJ deactivates, and the right column is the data taken 5 ms after the VGJ deactivates (as indicated by the jet profiles at the top of the figure). The black regions in the plots represent the turbine blade surface. In the x/d=10 plots the vortical structures are both clearly evident near a z/d of 6. The plots of x/d=15 and 20 are provided to demonstrate the structure of the vortex as it moves downstream towards the separation bubble. At x/d=25 the vortex can be seen interacting with the separation bubble. The plot in the left column depicts a dividing of the separation bubble, but no strong evidence of a vortical structure is visible. In the corresponding location in the right column (10 ms later), the vortical structure begins to take form at z/d=5. This development suggests that a distinct VGJ-induced vortical disturbance is being convected into the separation bubble.

Two iso-velocity surfaces ($U/U_{in}=0.75$) from the stereoscopic data are provided in Figure 3-11. These surfaces were taken from the same data used to provide the streamwise vorticity plots. Figure 3-11a is the iso-velocity surface immediately before the jet is turned off. The influence of the jet is clearly visible as it interacts with the separation bubble. It is interesting to note that at x/d=25 the bubble is beginning to divide near z/d=6. Figure 3-11b depicts the iso-surface immediately after the jet is turned off.

44
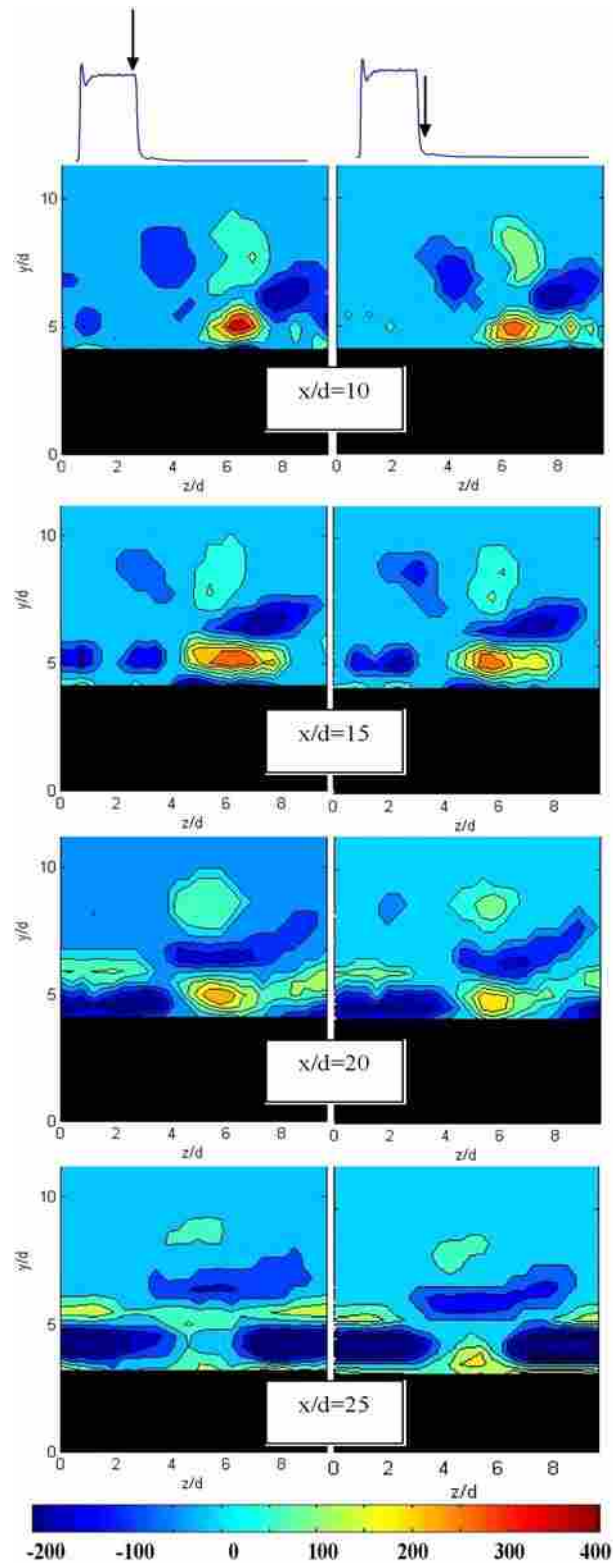
Figure 3-10: Streamwise vorticity comparison (10 ms apart) for VGJs only (Case 3). Jet profiles indicate location of data acquisition relative to VGJ pulse. VGJ at x/d=0 and z/d=9 (hole center). Blowing ratio, Bmax=2.
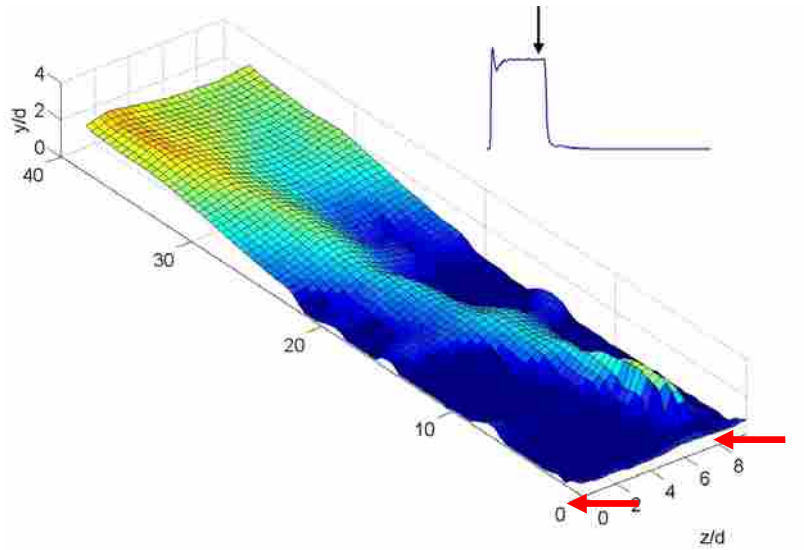
a. Iso-velocity surface (U/U_{in}=0.75) 5 ms before VGJ is deactivated
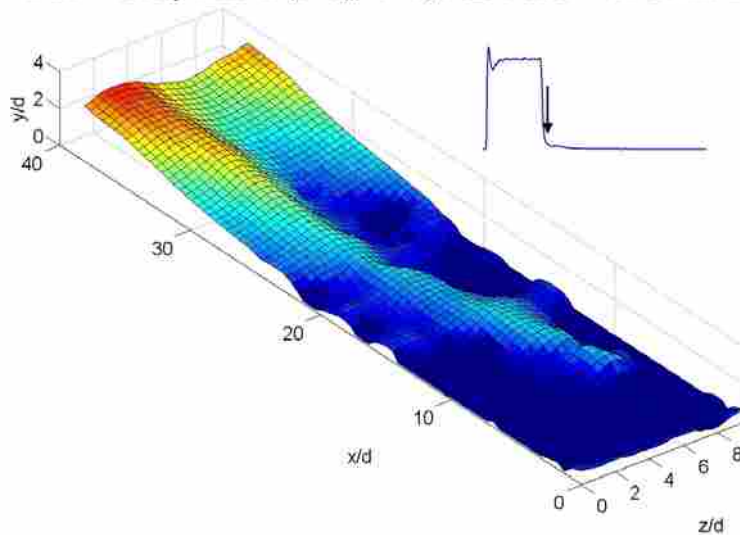
b. Iso-velocity surface (U/U_{in}=0.75) 5 ms after VGJ is deactivated.

Figure 3-11: Iso-velocity surfaces from stereoscopic PIV data depicting the impact of the VGJ (Case 3) on the separation bubble. The red arrows indicate an active jet (approximate location and orientation).

The depression in the separation bubble caused by the vortex has become more pronounced. The velocity surface on the left side of the depression (and vortex) begins to rise. This increased elevation is attributed to the vortex upwash or low momentum fluid being pulled into a higher momentum region. The downwash of the vortex causes the

46

depression in the separation bubble as high momentum fluid is carried into the low momentum bubble. Similar VGJ-induced boundary layer modifications have been observed by Hansen and Bons[22] and Khan and Johnston[23]. These data suggest that streamwise vortices also participate in the removal of the separation bubble. The three-dimensionality of the VGJ/bubble interaction in the stereoscopic data is also evident in the single camera PIV data.

4   A Preliminary Study of Wake and VGJ Synchronization

Prior to taking phase-locked PIV data of the wake-effected flow field, the jet duration, blowing ratio, and time delay (between the bar-triggered optical sensor signal and VGJ actuation) were adjusted to achieve the greatest extent of time-averaged separation bubble reduction. Cp distributions were used to measure the impact of each of these parameters over a range of values (time delays of 1, 50, 100, 150 and 200 ms, jet durations of 15, 30, and 50 ms, and blowing ratios of 1.7 and 2.5).

The effects of each of these parameters were isolated by holding two parameters constant while the third was adjusted over the specified range. The Cp distribution was monitored as the parameters were changed. Maximizing the jet duration (50 ms) and blowing ratio (2.5) clearly positively influenced the Cp distribution, reattaching the separation region. The time delay showed the greatest control near 150 ms.

The Cp comparisons led to the selection of a smaller range of parameters to be used for quantitative comparisons. The test matrix for the quantitative comparisons is presented in Table 1.

In order to quantify the relative merits of each of the eight cases presented in Table 1, the integrated boundary layer momentum flux losses (Γ) were calculated. The integrated boundary layer momentum flux losses are an adaptation to the integrated total pressure

Table 1: Test matrix for synchronization parameter study.

Case	Jet Duration (ms)	Time Delay (ms)	Blowing Ratio
No control (1)	-	-	-
Wakes only (2)	-	-	-
VGJs only (3)	50	N/A	2.5
4	50	50	2.5
5	50	100	2.5
6	50	150	2.5
7	50	150	1.7
8	30	150	2.5

measurements (found in Eq. 4.1) used by other researchers to quantify the losses associated with separation.[24]

$$\varphi = \int_{0}^{W} \frac{P_{T,in} - P_T(y)}{P_{T,in} - P_{S,in}} dy \tag{4.1}$$

The integrated total pressure measurements are made by traversing an anemometer across the full wake of the LPT. Full wake measurements are not possible on the control blade of the three blade cascade, since it is not a full blade. Assuming the total pressure remains constant outside the boundary layer (equal to $P_{tot,in}$) and the static pressure is constant across the boundary layer, Eq. 4.1 is reduced to Eq. 4.2. for steady incompressible flows.

This integrated boundary layer momentum flux loss parameter provides an estimate of total pressure loss in the suction surface boundary layer and was used to compare the relative momentum flux losses for each of the cases listed in the test matrix. Other

$$\Gamma = \int_0^\delta \frac{U_e{}^2 - U(y)^2}{U_{in}{}^2} dy \qquad (4.2)$$

modifications were also made to account for the non-uniform freestream velocity profiles. These modifications are outline in Olson et al.[25]

Several boundary layer velocity profiles were collected at the same location in the separation region (~87% axial chord) using a single-element hot-film. The hot-film velocity uncertainty was ±0.03 m/s. The profiles were taken near midspan four jet diameters above the bottom edge of a VGJ.

4.1   Time-Averaged Cp Distributions

Time-averaged Cp distributions (uncertainty in Cp of ±0.11) are presented in Figure 4-1 for four of the eight test cases in Table 1 (not shown are cases 4, 5, 7, and 8). The solid lines representing the VBI and MISES predictions are also included. In this Cp comparison the VBI is used as the benchmark of non-separated flow over the turbine, since it is for a high, non-separating Reynolds number. The MISES prediction is included because it is a better representation of the expected Cp distribution at lower Re numbers without control (no jets or wakes). Cp distributions that closely resemble the VBI are considered to be attached, while deviations from the VBI are indicative of boundary layer separation. The symbols represent the Cp from each static pressure tap along the suction and pressure surfaces of the Pack B blade for each test case.

The no control Cp data lie well below the VBI prediction. The separation zone is depicted by the relatively flat region in the Cp distribution from 70% to 90% axial chord.
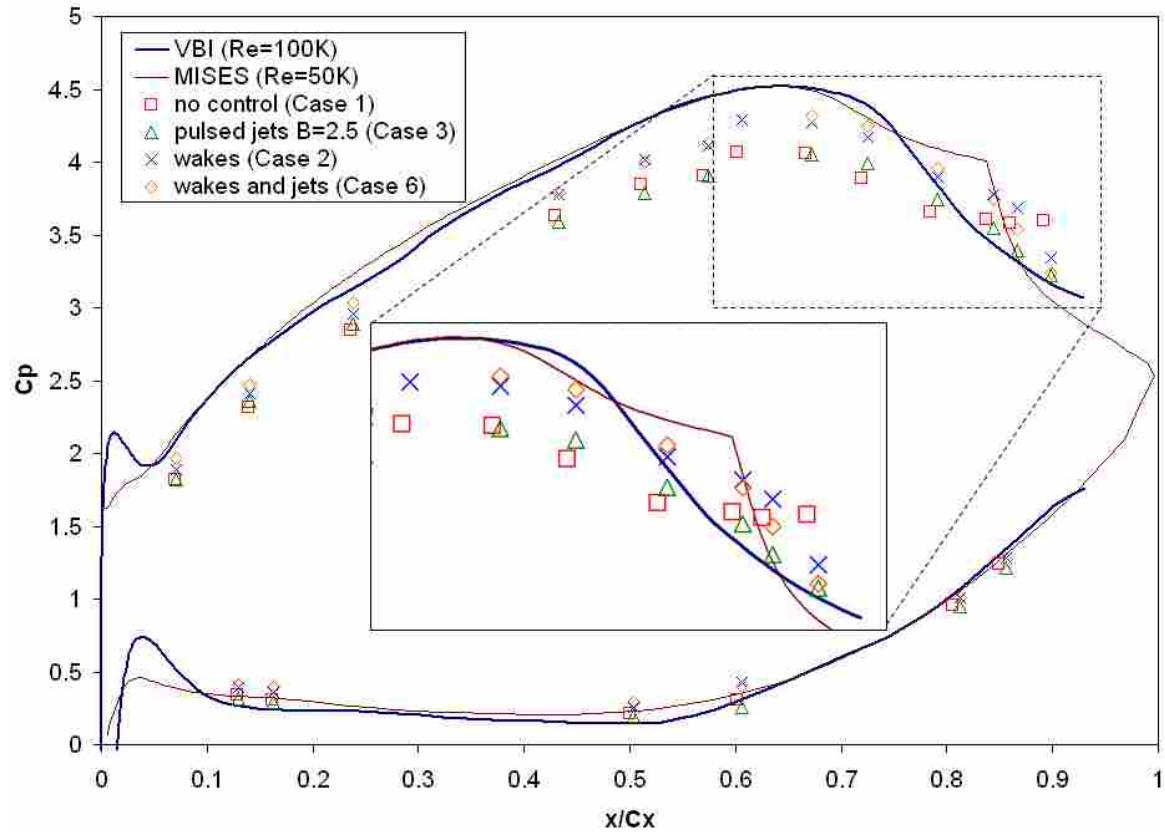
Figure 4-1: Experimental Cp distributions for the Pack B compared to the VBI. Plot includes no control (no wakes or jets), wake only, VGJ only, and combined wakes/jets data.

The introduction of unsteady VGJ control (case 3) eliminates a portion of this flattened region, suggesting reattachment of the separation bubble near 80% axial chord. For this case the VGJs had a blowing ratio of $B_{max}=2.5$, a jet duration of 50ms, and a duty cycle of 25% (where duty cycle is the ratio of jet duration to the period). The unsteady wake configuration (case 2) resembles the VBI more than the unsteady jet results in the region from 70% to 80% axial chord, but also has a larger deviation from 80% to 90% axial chord. The addition of VGJs to the unsteady wakes (case 6) further enhances the control achieved by the unsteady wakes or jets exclusively. This enhancement was seen over the entire range of the measured separation zone from 70% to 90% axial chord. As

52

mentioned earlier, the parameters used for the combined unsteady wake and jet Cp distribution in case 6 (B=2.5, jet duration=50 ms, time delay=150 ms) were determined following a rigorous optimization study.

4.2 Integrated Boundary Layer Momentum Flux Losses

The Cp distribution results suggest that synchronization of unsteady wakes and VGJs is beneficial but doesn't give any indication as to how sensitive these optimal conditions are to variations in the control variables. The integrated boundary layer momentum flux loss parameter (Γ) was used to quantify the control effectiveness. The normalized results are tabulated below in Table 2.

A comparison of the normalized boundary layer momentum flux loss parameters for wakes only and VGJs only (Γ/Γ_o = 0.75 vs. 0.68 respectively) shows that unsteady VGJs have a more pronounced impact on the momentum flux losses (separation region). This was an unexpected result given that the unsteady wake disturbance is a spanwise event

Table 2: Normalized results from the integrated boundary layer mometum flux loss parameter.

Case	Jet Duration (ms)	Time Delay (ms)	Blowing Ratio	Γ/Γ_o
No control (1)	-	-	-	1
wakes only (2)	-	-	-	0.75
VGJs only (3)	50	N/A	2.5	0.68
4	50	50	2.5	0.65
5	50	100	2.5	0.62
6 (Optimum)	50	150	2.5	**0.55**
7	50	150	1.7	0.63
8	30	150	2.5	0.59

while the VGJ disturbance is not. However, since the z/d location where the boundary layer (and thus Γ) data were taken aligned directly with the VGJ trajectory (z/d =6), it is expected that the relative advantage of the VGJ only case would decrease if the same measurements were taken at other z/d locations less influenced by the jet. This is due to the three-dimensionality of the VGJ disturbance and its effect on the separation bubble dynamics, as will be shown later.

A number of other important synchronization factors can be gleaned from this study. Three time delays were tested while holding the jet duration and blowing ratio constant. It is evident that the largest time delay (150 ms) resulted in the greatest momentum flux loss reduction [Case 6 (Γ/Γ_o=0.55) compared to Case 5 (Γ/Γ_o=0.62) and Case 4 (Γ/Γ_o=0.65)]. This would suggest that the timing between the passing wake and the VGJ disturbances is an important factor in identifying an optimal synchronization condition.

Once the "optimal" time delay was determined, a study was performed to identify the separation bubbles' dependence on the jet duration. Jet durations of 50 ms and 30 ms were compared and resulted in the flux losses, 0.55 and 0.59 respectively. Jet durations larger than 50 ms were not studied to maintain low mass flow requirements. These results suggest that jet duration also has an impact on the flux losses. This corroborates the results obtained in chapter 3 using the 5 Hz and 3 Hz VGJ pulse histories.

The final parameter that was adjusted was the blowing ratio. A blowing ratio of 2.5 was shown to be significantly more effective at reducing the total pressure losses due to the separation bubble. Higher blowing ratios were not studied because the maximum allowable pressure on the inline solenoid valve was near B_{max}=2.5.

5 Synchronized Unsteady Wakes and Jets

5.1 Iso-Velocity Surfaces for Wakes and Jets

Once an optimal synchronizing configuration was obtained, PIV measurements were taken to identify the flow physics responsible for the reduced momentum flux losses. Comparisons of the wake and jet disturbances were also made. Figure 5-1 contains iso-surfaces of the velocity magnitude computed using the single camera PIV data.

An iso-velocity surface of U/U_{in}=1.0 was selected because it clearly depicts the distinct influences of the passing wake and jet. Each of the 15 data acquisition times is represented in the figure, depicting the separation bubble's behavior over the complete period. Figure 5-1 also includes an iso-velocity surface without wakes or VGJs for comparison (labeled No Control). These surfaces give an indication of the jet and wake effects on the flow. In order to facilitate identification of the separation bubble, the curvature of the turbine blade was removed from the iso-velocity surface height. Thus, the vertical axis (y/d) represents the distance from the iso-velocity contour to the blade surface. Accordingly, elevated portions of the iso-velocity surface are attributed to the separation bubble. The flow moves from right to left as x/d extends from 0 to 67 (approximately 59% to 100% axial chord). The VGJ is located near a z/d of 9 (hole center) but is only active in the range of t/T_{wake}=0.71-0.84.
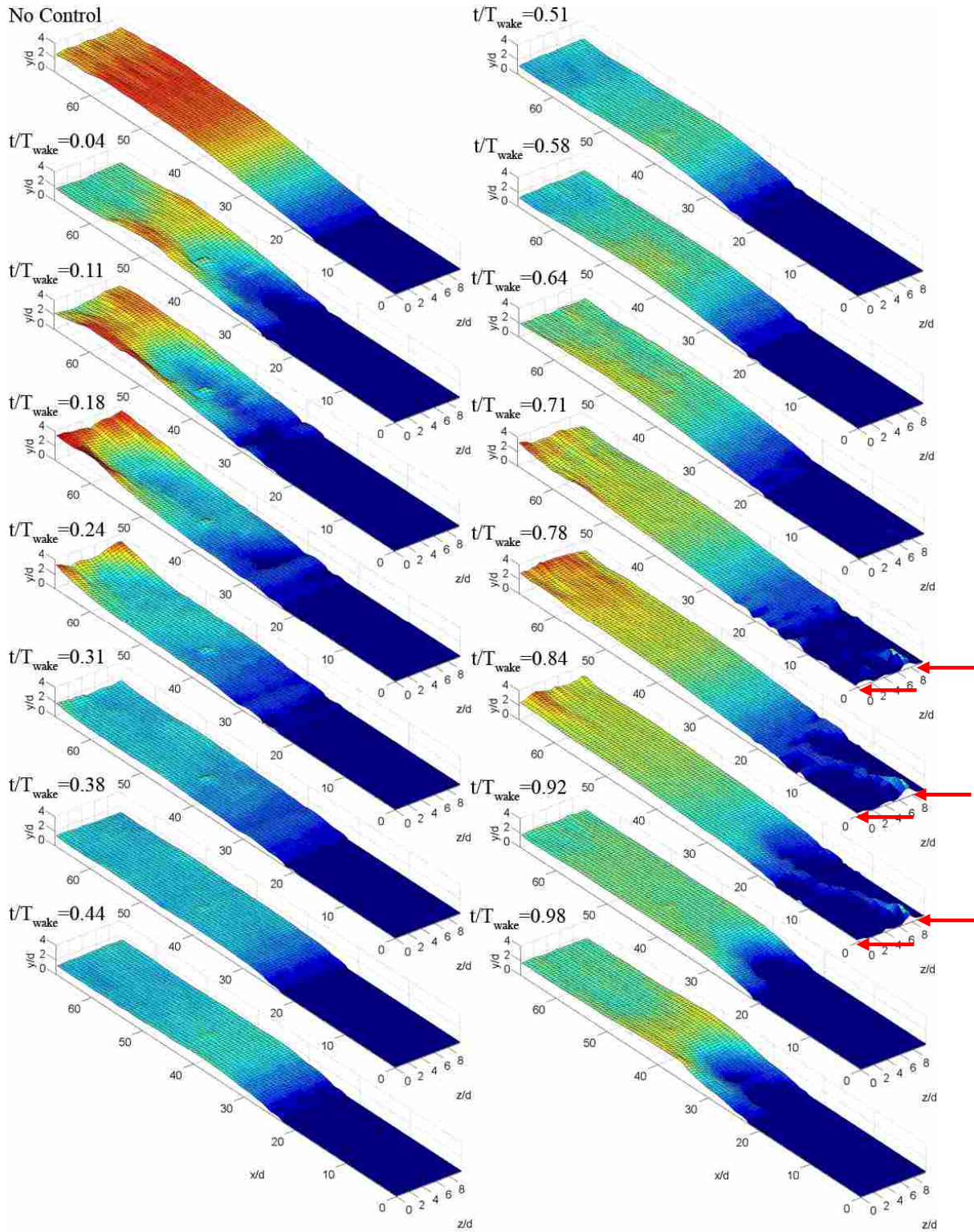
Figure 5-1: Phase-locked iso-velocity surfaces (U/U$_{in}$=1.0) for wakes/jets (Case 6) configuration. Red arrows indicate approximate jet locations.

A caricature of the approximate position of the wake disturbance in the cascade section is provided in Figure 5-2 for each of the time locations of data acquisition in Figure 5-1.
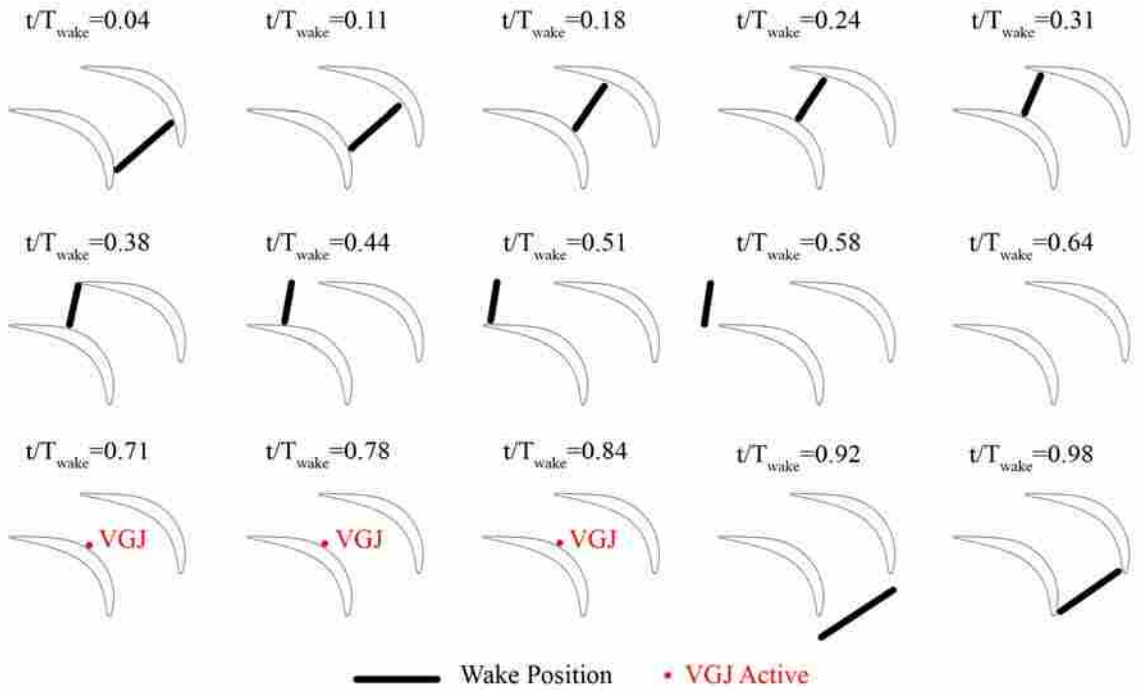
Figure 5-2: Approximate wake location in the cascade.

The solid black lines in the figure represent the wake position. The red dots are used to indicate that the VGJs are active. This figure is provided to help the reader identify the individual effects of the unsteady wakes and the VGJs on the separation bubble.

Since t/T_{wake}=0 is referenced to the passing of the rod through the optical sensor, indication of a passing wake isn't immediately evident in the iso-velocity surfaces of Figure 5-1. At t/T_{wake}=0.04 the lingering effects of a VGJ/separation bubble interaction are still present. This VGJ pulse occurred $\Delta t/T_{wake}$= 0.29 (65 ms) prior to the passing of the rod through the optical sensor (it is therefore phase-locked to the previous rod

passing). The VGJ has caused the separation bubble to reattach at the upstream end. The higher momentum fluid in the reattached region meets the slow moving separation bubble and causes an elevated bulge in the iso-velocity surface. This bulge convects off the end of the blade in subsequent data sets. The three-dimensional effect of the VGJ on the separation bubble is still very apparent as the separation bubble moves off the blade in t/T_{wake} of 0.11, 0.18, and 0.24.

Once the separation bubble is ejected from the blade ($t/T_{wake}= 0.24$), there is a period of time before the bubble begins to recover. The iso-velocity surfaces at t/T_{wake} of 0.31, 0.38, and 0.44 show very little growth in the separation region. By $t/T_{wake}=0.51$ the boundary layer begins to separate again. Figure 5-1 also suggests that at this same period of time the wake disturbance begins to influence the separation bubble. This is evidenced by a two-dimensional rise in the separation bubble near $x/d=40$. The wake-induced 2D bunching is not as dramatic as the jet-induced bunching seen at $t/T_{wake}=0.04$, but this event also propagates downstream re-energizing the separated boundary layer. The wake-induced disturbance propagates off the blade near $t/T_{wake}=0.84$. During this same period of time, the VGJs are influencing the upstream end of the separation zone.

5.2   Wakes Only Iso-Velocity Surfaces (PIV)

Given the difficulty in distinguishing the wake and jet induced disturbances in the iso-velocity surfaces of Figure 5-1, PIV data were also collected without the VGJ disturbance. These data are used to isolate the impact of the wake disturbance on the separation bubble. These data are presented in the form of iso-velocity surfaces ($U/U_{in}=1.0$) found in Figure 5-3.
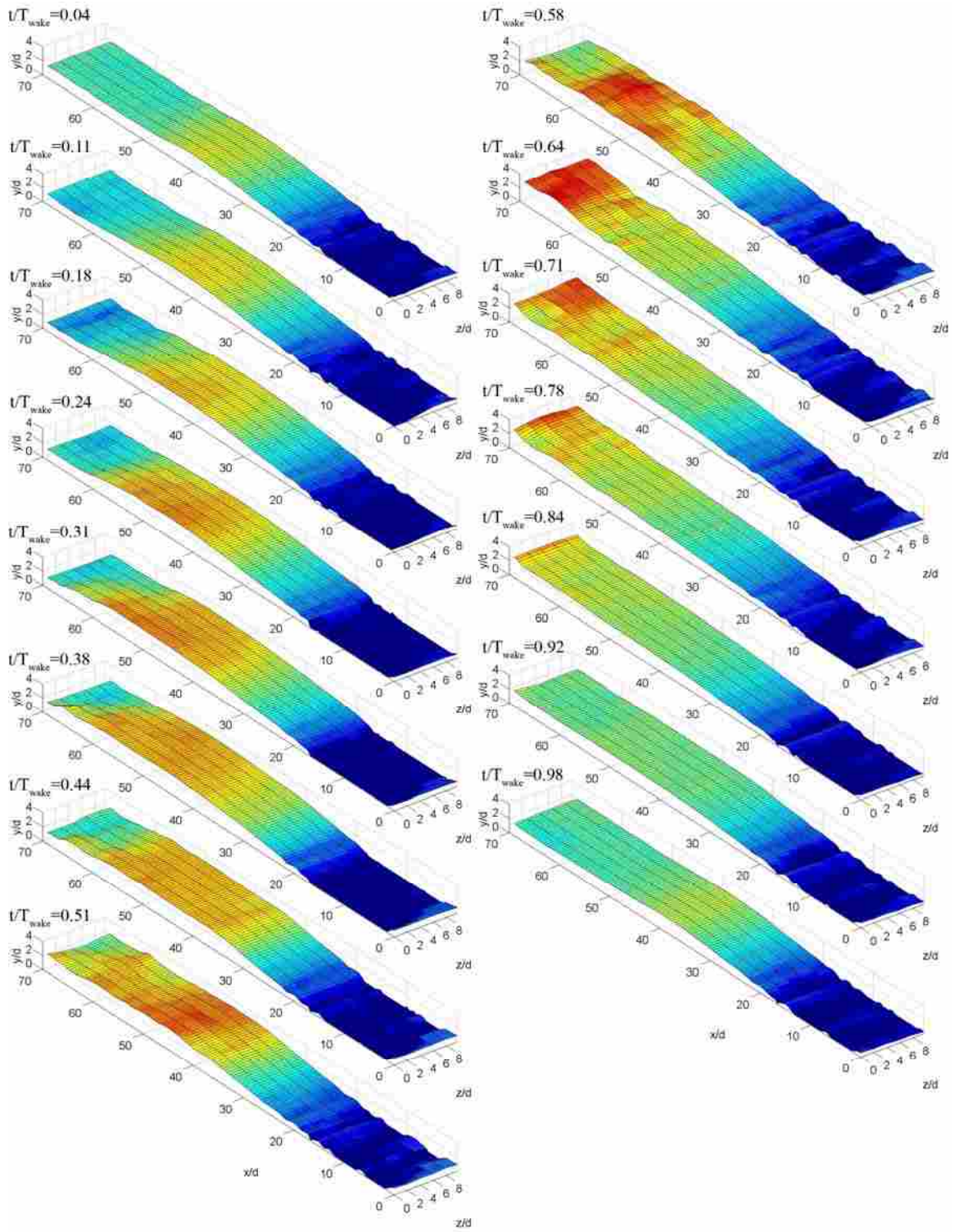
58

Figure 5-3: Iso-velocity surface U/U$_{in}$=1.0 for wakes only data (Case 2).

59

The iso-velocity surfaces from the wakes only data depict the events outlined in the discussion of the wakes and jets data. From t/T_{wake} of 0.04 to 0.44 the separation bubble recovers from the previous wake disturbance. This differs from the jets and wakes data depicted in Figure 5-1 because there is no VGJ-induced disturbance affecting the separation region. A two dimensional bunching of the separation bubble is evident at t/T_{wake}=0.51 between x/d=40 and x/d=50. In the subsequent iso-velocity surfaces this 2D bulge convects downstream. By t/T_{wake}=0.84 this disturbance has propagated off the blade leaving a smaller separation bubble. The relative impact of the synchronized wakes with jets and the wakes only data will be investigated further.

5.3   Blade Follower Results

U_{rms}/U_{in} data are presented in Figure 5-4 to further help identify the effects of the wake and jet disturbances. Figure 5-4 is divided into 24 plots representing 24 phase-locked data windows taken over the wake-passing period (T). Similar to the PIV data, the hot-film data were phase-locked using the rod optical sensor. The non-dimensional time is shown in the upper right corner of each plot. The use of U_{rms}/U_{in} plots assists in the identification of the separated flow region, the pulsed jet trajectory, and (to a lesser extent) the wake trajectory. From t/T_{wake}=0.04 to 0.25 the separation bubble ($x/C_x > 0.8$) is decreasing in size due to the influence of the previous VGJ disturbance. The wake disturbance (shown as a red arrow) then enters the measurement domain as evidenced by a slight increase in freestream turbulence upstream of the separation bubble. The separation bubble is further reduced in size due to the passing of the wake (t/T_{wake}=0.54

60
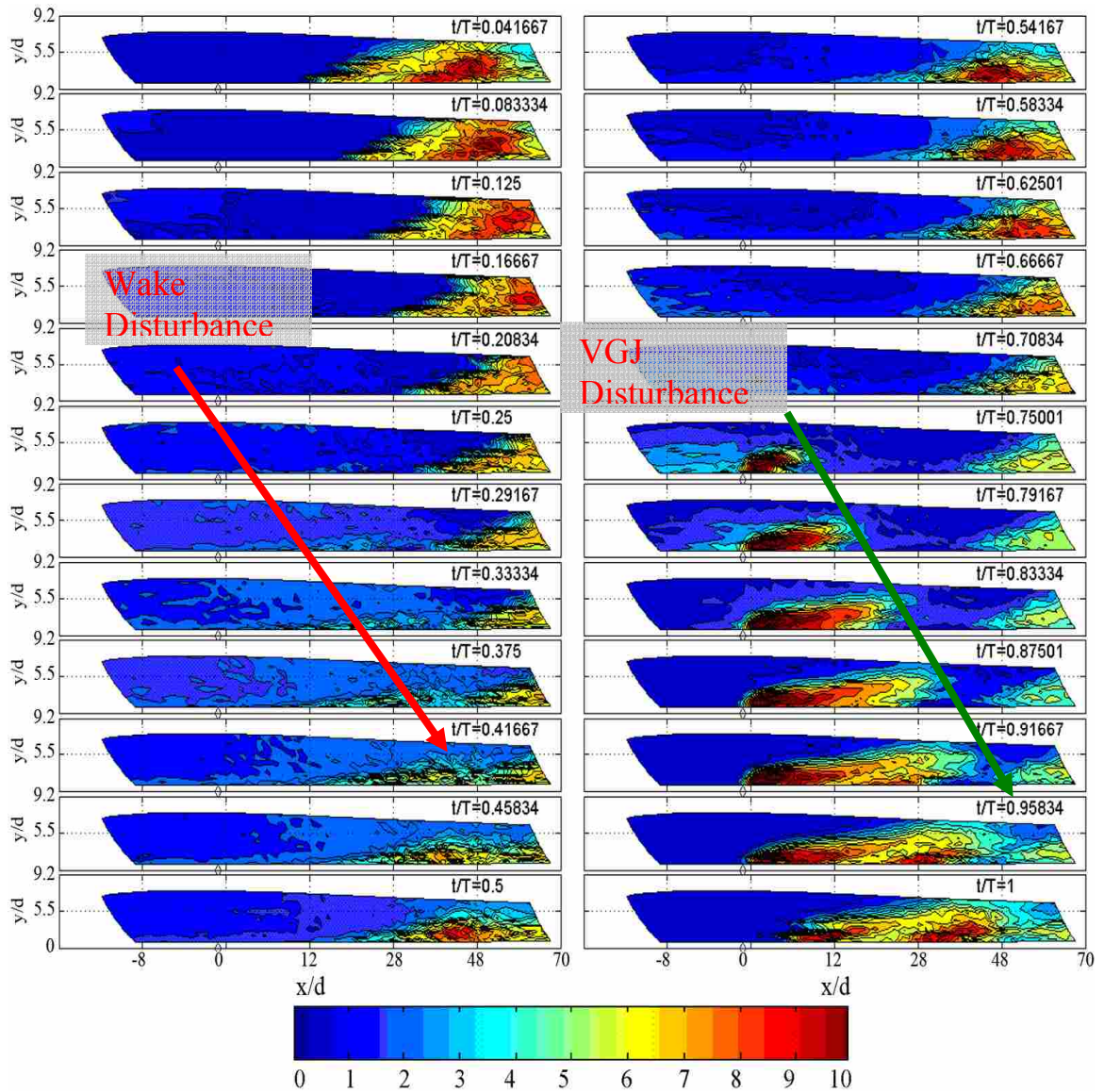
Figure 5-4: U_{rms}/U_{in} plots of the wakes/jets (Case 6) configuration. The non-dimensional time is labeled in the upper right corner of each plot.

to 0.71). Once the wake has passed, there remains a region of low turbulence referred to by Gostelow et al. [13] as a "calmed zone". This region of low turbulence is seen at the trailing edge ($x/C_x > 0.9$) from $t/T_{wake}=0.75$ until the influence of the jet disturbance arrives (green arrow).

61

5.4   Time-History Plots (Hot-Film)

This calmed zone is further evident in the time history plot at y/d=0.80 presented in

Figure 5-5a.
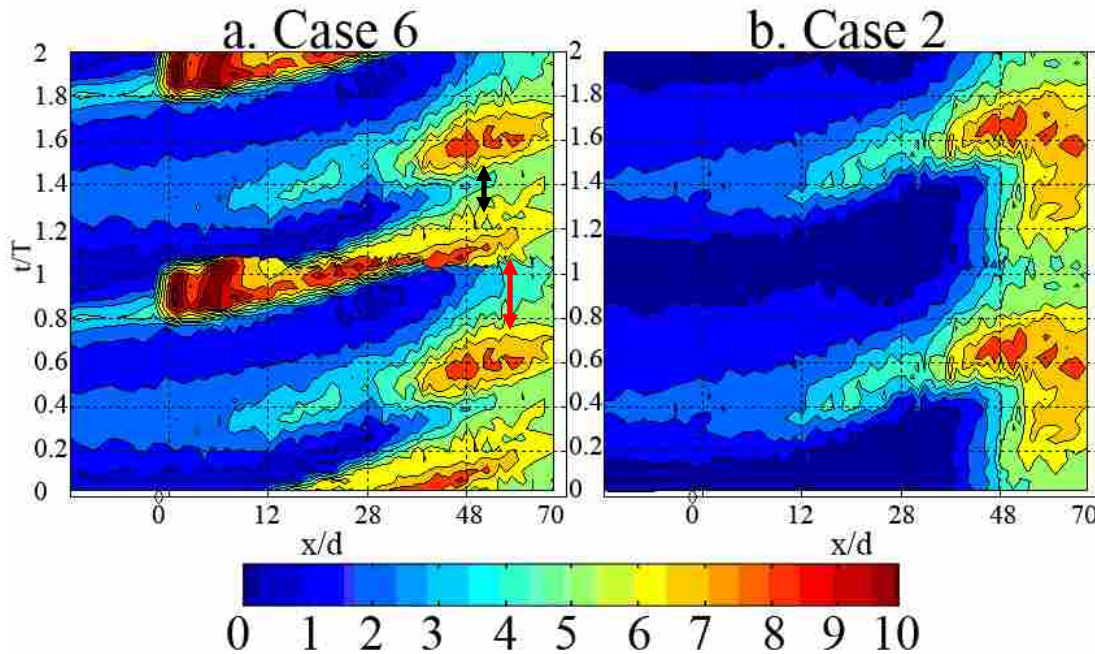
Figure 5-5: Time history plots (U$_{rms}$/U$_{in}$) depicting wake with jet and wake only interactions with the separation bubble. The calmed zones induced by the wake and VGJ are marked with red and black arrows respectively. The VGJs are located at 59% Cx.

These plots depict the time history of the U$_{rms}$/U$_{in}$ for a range of streamwise locations, while the hot-film is maintained at a constant wall distance and z/d. The two-sided red arrow identifies the calmed zone that results from the wake disturbance. The smaller black arrow identifies the calmed zone that results from the VGJ disturbance. Figure 5-5b is the time history plot for the wakes only case. In the absence of an intermediate jet disturbance, this plot shows bubble regrowth (U$_{rms}$/U$_{in}$> 5%) beginning at t/T$_{wake}$=1.1. It appears that the VGJ disturbance arrives at the separation bubble just prior to the

breakdown of the calmed zone caused by the wake. This new disturbance prevents regrowth of the separation bubble and produces another calmed zone. A short time later a new wake disturbance reestablishes the wake induced calmed zone and the cycle continues.

These figures suggest that the optimal synchronization of jets and wakes prolongs the calmed zone and suppresses separation bubble regrowth. In order to optimize the control of wakes/jets, the jet disturbance should interact with the separation zone just prior to the end of the wake-induced calm zone.

5.5 Integrated Average Iso-Velocity Surfaces

After the wake passes in the plot of t/T_{wake}=0.91, there is a significantly larger separation bubble in comparison to the residual bubble after the jet disturbance (t/T_{wake}=0.31-0.51). In order to quantify the size of the separation bubbles at each t/T, each iso-velocity surface from Figure 5-1 was averaged in the spanwise direction. The resultant average iso-velocity surfaces were then integrated and normalized by the no control case. Figure 5-6 is a plot of this integrated measurement for each of the non-dimensional times (synchronized wakes with jets and wakes only data).

This figure shows the impact of each of the disturbances and their relative effectiveness in suppressing the separation bubble. The configuration with wakes only causes a decrease in the normalized separation zone from 0.94 to 0.72. At t/T_{wake}=0.78 the normalized separation bubble grows to nearly 0.81 as the 2D wake disturbance impacts it. The bubble size then decreases to 0.58 as the 2D disturbance is ejected from
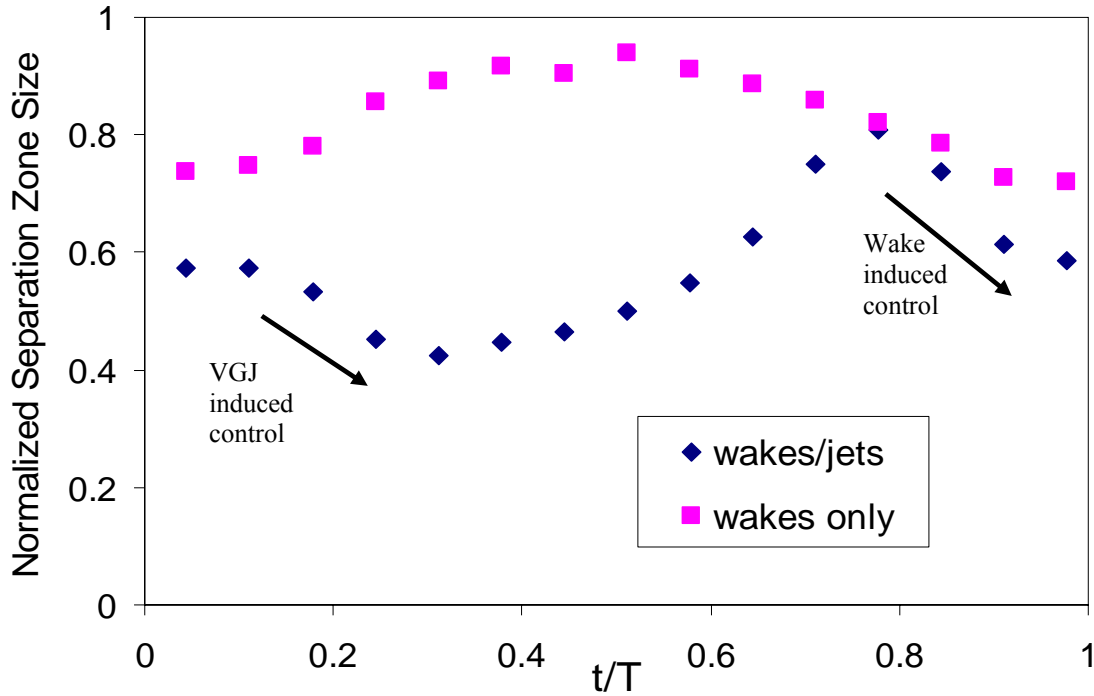
Figure 5-6: Integrated iso-velocity surfaces (wakes/jets and wakes only) at each data acquisition time. The data were normalized by the size of the no control separation bubble. Case 6 (wakes/jets) and Case 2 (wakes only).

the blade. The average size of the separation bubble decreases very rapidly as evidenced by the slope of the line during wake induced control. A slower reduction is noted in the VGJ induced control. A comparison of the speed and size of these reductions indicates that the spanwise-average wake induced control might actually have more impact than the jet. After the wake passes, the jet disturbance interacts with a partial separation bubble. The remainder of the low momentum fluid is reenergized, further decreasing the separation bubble to 0.42 (0.3 less than the wakes only configuration). These results suggest that at the optimal synchronizing configuration the wake disturbance prepares the separation bubble for maximum jet effectiveness.

6 Conclusions

Phase-locked PIV measurements were made for two distinct VGJ pulsing signals. The VGJ pulsing frequencies were varied to isolate the influences of jet initiation, relaxation, and duration on the separation bubble. It was shown that the control achieved was due to boundary layer transition and streamwise vortical structures caused by the VGJs. Stereoscopic PIV data showed that the three-dimensional shape of the jet-disturbed separation bubble coincided with the location of a streamwise vortical structure. The depression and elevated regions in the separation bubble corresponded with the downwash and upwash of the vortical structure respectively. The duration of the jet and the jet relaxation time were important factors in determining the extent of control. This was attributed to both the time required for the transition to penetrate from the free shear layer into the separation zone and the initial size of the separation bubble.

Surface static pressure and hot-film data were used to identify "optimal" conditions for the synchronization of VGJ and wake disturbances. Results suggest that jet duration, blowing ratio, and the time delay between disturbances all have a significant impact on control effectiveness. Maximum control was achieved with a blowing ratio of 2.5, a jet duration of 50 ms, and a time delay of 150 ms.

Single camera PIV and hot-film data were used to identify the relative impacts of the two unsteady disturbances and the flow physics that resulted in the control effectiveness.

The data were used to show that the wake and jet disturbances produced calmed zones. At optimal conditions, the jet disturbance arrived at the separation bubble just prior to the breakdown of the wake-induced calmed zone. Consequently, the jet disturbance interacted with a smaller separation bubble. This resulted in the most substantial removal of the separation zone. Synchronized wakes with jets were shown to reduce the separation bubble more than unsteady wakes alone.

Given that this research was a preliminary study of synchronized wakes with jets, future work is recommended to more accurately identify the optimal synchronization parameters (blowing ratio, time delay, jet duration) and further explore the unsteady wake and unsteady jet interaction. Also, it is recommended that stereoscopic PIV data be taken to validate the turbulence statistics collected with the hot-film. This will require a significant increase in the amount of images taken.

7 References

[1]Mayle, R.E., 1991, "The Role of Laminar-Turbulent Transition in Gas Turbine Engines," ASME *Journal of Turbomachinery*, Vol. 113, pp. 509-537.

[2]Sondergaard, R., Bons, J.P., and Rivir, R. B., 2002, "Control of Low-Pressure Turbine Separation Using Vortex Generator Jets," *AIAA J. Propulsion and Power*, Vol. 18, No. 4, pp.889-895. Jul/Aug 2002.

[3]Sharma, O., 1998, "Impact of Reynolds Number of LP Turbine Performance," *Proc. Of 1997 Minnowbrook II Workshop on Boundary Layer Transition I Turbomachines*, NASA/CP-1998-206958, pp. 65-69.

[4]Matsunuma, T., Abe, H., Tsutsui, Y., and Murata, K., 1998, "Characteristics of an Annular Turbine Cascade at Low Reynolds Numbers," presented at IGTI 1998 in Stockholm, Sweden, June 1998, 98-GT-518.

[5]Lake, J.P., King, P.I., and Rivir, R.B., 2000, "Low Reynolds Number Loss Reduction on Turbine Blades with Dimples and V-Grooves," AIAA Aerospace Sciences Meeting and Exhibit, AIAA 00-0738.

[6]Bons, J.P., Sondergaard, R., Rivir, R.B., 2001, "Turbine Separation Control Using Pulsed Vortex Generator Jets," ASME Journal of Turbomachinery, Vol. 123, pg. 198-206.

[7]Eldredge, R. G., and Bons, J. P., 2004, "Active Control of a Separating Boundary Layer with Steady Vortex Generating Jets—Detailed Flow Measurements," presented at the AIAA Aerospace Sciences Meeting, Reno, Nevada, 5-8 Jan. 2004, AIAA 2004-0751.

[8]Hansen, L. C. and Bons J. P., 2004, "Time-Resolved Flow measurements of Pulsed Vortex-Generator Jets in a Separating Boundary Layer," presented at the 2nd AIAA Flow Conference in Portland, OR, 28 June- 1 July 2004, AIAA 2004-2203.

[9]Postl, D., Gross, A., and Fasel, H. F., 2003, "Numerical Investigation of Low-Pressure Turbine Blade Separation Control," AIAA Aerospace Sciences Meeting and Exhibit, Reno, NV, 6-9 Jan. 2003, AIAA 2003-0614.

[10]Bons, J.P., Sondergaard, R., and Rivir, R. B., "The Fluid Dynamics of LPT Blade Separation Control Using Pulsed Jets," *ASME Journal of Turbomachinery*, Vol. 124, Jan. 2002, pp. 77-85.

[11]Volino, R. J., 2003, "Separation Control on Low-Pressure Turbine Airfoils Using Synthetic Vortex Generator Jets," *Proceedings of ASME Turbo Expo 2003: Power for Land, Sea, and Air,* GT2003-38729.

[12]Stieger, R., Hollis, D., Hodson, H., 2003, "Unsteady Surface Pressures Due to Wake Induced Transition in a Laminar Separation Bubble on a LP Turbine Cascade," *Proceedings of ASME Turbo Expo 2003: Power for Land, Sea, and Air,* GT2003-38303.

[13]Gostelow, J.P. and Thomas, R.L., 2003, "Response of a Laminar Separation Bubble to an Impinging Wake," *Proceedings of ASME Turbo Expo 2003: Power for Land, Sea, and Air,* GT2003-38972.

[14]Funazaki, K., Yamada, K., Ono, K., Segawa, K., Hamazaki, H., Takahashi, A., and Tanimitsu, H., 2006, "Experimental and Numerical Investigations of Wake Passing Effects upon Aerodynamic Performance of a LP Turbine Linear Cascade With Variable Solidity," *Proceedings of ASME Turbo Expo 2006: Power for Land, Sea, and Air,* GT2006-90507.

[15]Cattanei, A., Zunino, P., Schroder, T., Stoffel, B., and Matyschok, B., 2006, "Detailed Analysis of Experimental Investigations on Boundary Layer Transition in Wake Disturbed Flow," presented at the 2006 IGTI conference in Barcelona, 8-11 May 2006, GT2006-90128.

[16]Eldredge, R. G., and Bons, J. P., 2004, "Active Control of a Separating Boundary Layer with Steady Vortex Generating Jets—Detailed Flow Measurements," presented at the AIAA Aerospace Sciences Meeting, Reno, Nevada, 5-8 Jan. 2004, AIAA 2004-0751.

[17]Rao, K.V., Delaney, R.A., and Topp, D.A., 1994, "Turbine Vane-Blade Interaction: Vol. 1, 2-D Euler/Navier-Stokes Aerodynamic and Grid Generation Developments," U.S. Air Force Research Lab., Rept. WL-TR-94-2073, Wright-Patterson AFB, OH, Jan. 1994.

[18]Bons, J. P., Hansen, L. C., Clark, J. P., Koch, P. J., Sondergaard, R., 2005 "Designing Low-Pressure Turbine Blades with Integrated Flow Control," *Proceedings of ASME Turbo Expo 2005: Power for Land, Sea, and Air,* GT2005-68962.

[19]LaVision, 2004, "Davis Flowmaster," v. 7.0, March 2004, LaVision GmbH, Anna-VandenHoeck-Ring 19, D-37081 Gottingen.

[20]Bons, J.P., Bloxham, M. and Reimann, D., 2006, "Separated Flow Transition on an LP Turbine Blade with Pulsed Flow Control," presented at the 2006 IGTI conference in Barcelona, 8-11 May 2006, GT2006-90754.

[21]Reimann, D., Bloxham, M., Crapo, K., Pluim, J., Bons, J.P., "Influence of Vortex Generator Jet-Induced Transition on Separating Low Pressure Turbine Boundary Layers," AIAA Fluid Dynamics Conference, San Francisco, 5-8 June 2006, AIAA 2006-2852.

[22]Hansen, L. C. and Bons J. P., 2006, "Phase-Locked Flow Measurements of Pulsed Vortex-Generator Jets in a Separating Boundary Layer," *AIAA Journal of Propulsion and Power,* Vol. 22, No 3, May-June 2006, pp. 558-566.

[23]Khan, Z. U. and Johnston, J. P. "On Vortex Generating Jets," *International Journal of Heat and Fluid Flow*, Vol. 21, pp. 506-511. 2000.

[24]Sondergaard, R., Bons, J. P., and Rivir, R. B., "Control of Low-Pressure Turbine Separation Using Vortex-Generator Jets," *AIAA Journal of Propulsion and Power,* Vol. 18, No. 4, pp. 889-895, Jul/Aug 2002.

[25]Olson, D.H., Reimann, D., Bloxham, M., Bons, J.P., "The Effect of Elevated Freestream Turbulence on Separation Control with Vortex-Generating Jets," presented at the AIAA 43rd Aerospace Sciences Meeting and Exhibit, Reno, Nevada, 10-13 Jan. 2005, AIAA 2005-1114.

[26]Bloxham, M., Reimann, D., Bons, J.P., 2006, "The Effect of VGJ Pulsing Frequency on Separation Bubble Dynamics," presented at the AIAA 44th Aerospace Sciences Meeting and Exhibit, Reno, Nevada, 9-12 Jan. 2006, AIAA 2006-0876.

Appendix: Uncertainty Analysis

Assumptions
P = 88000 Pa
T = 300 K
R = 287 J/kgK
ρ = 1.022 kg/m^3
ΔP = 0.1 "H$_2$O (maximum allowed differential pressure for Druck calculations)
U$_{max}$ = 3 m/s   (maximum expected velocity through tunnel)
U$_{in}$=1.54 m/s   (cascade inlet velocity)
PM= 8 pixels (8 pixels of particle motion for PIV)

Uncertainty in Density:

Resolution Uncertainties for density calculation
u_P = ± 47.9 Pa
u_T = ± 0.05 K

$$\rho = P\big/RT$$

$$u_\rho = \sqrt{\left(\frac{\partial \rho}{\partial P} u_P\right)^2 + \left(\frac{\partial \rho}{\partial T} u_T\right)^2}$$

$$u_\rho = \sqrt{\left(\frac{1}{RT} u_P\right)^2 + \left(-\frac{P}{RT^2} u_T\right)^2}$$

$$u_\rho = \textbf{0.001 kg/m}^3$$

Uncertainty in the Inlet Velocity from 0.1" Druck Differential Pressure Transducer

Uncertainty in the Manometer used to Calibrate Druck
average H$_2$0   0.0525
resolution   0.001
u_{mano}= 0.001/0.0525 = 0.019

Table 3: Druck calibration data points

Voltage	Meas. inH20	Pred. inH20	(Meas-Pred)^2
2.99	0	0.00294954	8.69981E-06
3.47	0.015	0.01267223	5.4185E-06
4.14	0.03	0.02624348	1.41114E-05
5.14	0.045	0.04649908	2.24725E-06
5.95	0.06	0.06290612	8.44553E-06
6.51	0.075	0.07424926	5.63617E-07
7.5	0.09	0.0943023	1.85098E-05
7.79	0.105	0.10017642	2.32669E-05

$y = 0.0202556x - 0.0576147$

$R^2 = 0.9914008$
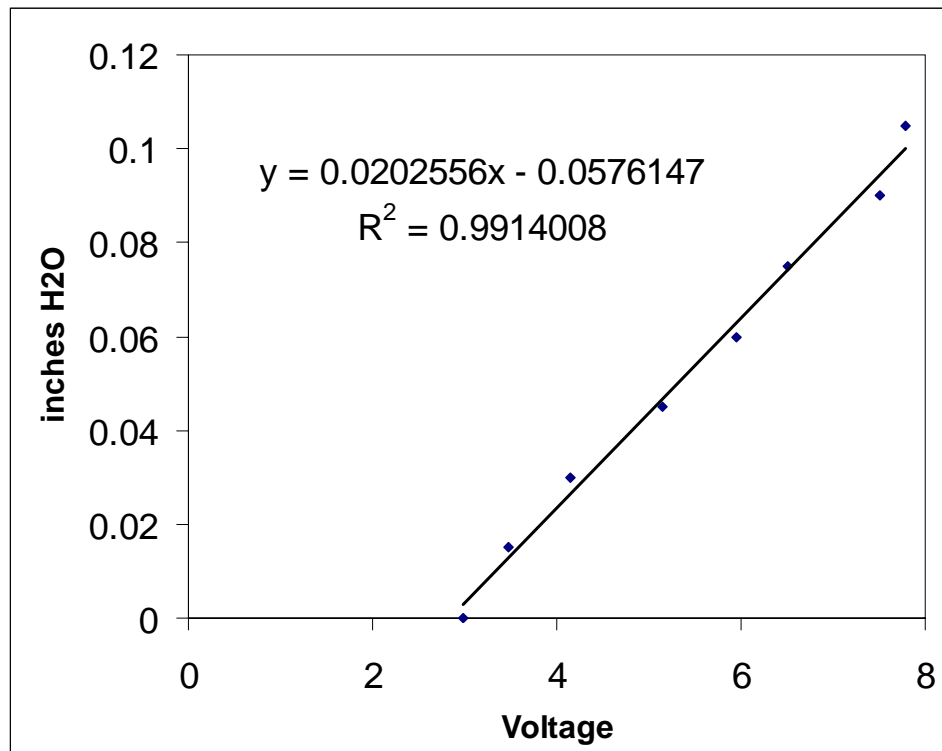
Appendix-1: Calibration curve for the Druck differential pressure transducer.

$$S_{yx} = \sqrt{\dfrac{\sum\limits_{i=1}^{n}(meas\_H20 - pred\_H20)^2}{n-1}} \quad \text{(standard error of the curve fit)}$$

$S_{yx} = 0.0034$

$t_{7,0.95} = 2.365$ (t statistic for 95th percentile)

$u_{curve} = \pm t_{7,0.95} S_{yx} = 0.0081$

$u_{cal} = \sqrt{u_{mano}^2 + u_{curve}^2}$ (uncertainty in calibration of Druck)

$u_{cal} = 0.021$

Uncertainties provided by Druck
non-linearity (u_{NL})   0.005
hysteresis (u_H)   0.0025
repeatability (u_R)   0.0025
~~Temp. Range~~   neglect (temperature is constant)
~~Long Term Stability~~   neglect (each set of data was taken over a short period of time)

$$V = \sqrt{\dfrac{2\Delta P}{\rho}}$$

$$u_{vel} = \sqrt{\left(\dfrac{\partial V}{\partial \Delta P}u_{cal}\right)^2 + \left(\dfrac{\partial V}{\partial \rho}u_{\rho}\right)^2 + \left(U_{FS}*u_{NL}\right)^2 + \left(U_{FS}*u_{H}\right)^2 + \left(U_{FS}*u_{R}\right)^2}$$

$$u_{vel} = \sqrt{\left(\sqrt{\dfrac{1}{2\rho\Delta P}}u_{cal}\right)^2 + \left(-\sqrt{\dfrac{\Delta P}{2\rho^3}}u_{\rho}\right)^2 + \left(U_{FS}*u_{NL}\right)^2 + \left(U_{FS}*u_{H}\right)^2 + \left(U_{FS}*u_{R}\right)^2}$$

$u_{vel} = 0.19$ m/s (Uncertainty in inlet velocity)

Uncertainty in Cp

$$Cp = \dfrac{P_{Tot,in} - P}{P_{Tot,in} - P_{s,in}}$$

$$Cp = \frac{U^2}{U_{in}^2}$$

$$u_{Cp} = \sqrt{\left(\frac{\partial Cp}{\partial U}u_{vel}\right)^2 + \left(\sqrt{\frac{\partial Cp}{\partial U_{in}}}u_{vel}\right)^2}$$

$$u_{Cp} = \sqrt{\left(\frac{2U}{U_{in}^2}u_{vel}\right)^2 + \left(\frac{-2U^2}{U_{in}^3}\right)^2}$$

$u_{Cp} = 0.104$

Uncertainty in velocity with hot-film

$u_{King} = 0.012$ (uncertainty from King's Law curve fit)

$$u_{film} = \sqrt{u_{King}^2 + u_{vel}^2} \quad \text{(uncertainty of the hot-film)}$$

$u_{film} = 0.022$ m/s

Uncertainty in velocity with PIV

From LaVision calibration
$u_{Pixel} = 0.2$ pixels

$$u_{PIV} = \sqrt{u_{vel}^2 + \left(\frac{U_{FS} * u_{pixel}}{PM}\right)^2} \quad \text{(uncertainty of the PIV)}$$

$u_{PIV} = 0.08$ m/s